

# Mode-Coupling Analysis of $^{15}\text{N}$ CSA– $^{15}\text{N}$ – $^1\text{H}$ Dipolar Cross-Correlation in Proteins. Rhombic Potentials at the N–H Bond

Eva Meirovitch,<sup>\*,†</sup> Yury E. Shapiro,<sup>†</sup> Vitali Tugarinov,<sup>†,‡</sup> Zhichun Liang,<sup>§</sup> and Jack H. Freed<sup>\*,§</sup>

Faculty of Life Sciences, Bar-Ilan University, Ramat-Gan 52900, Israel, Baker Laboratory of Chemistry and Chemical Biology, Cornell University, Ithaca, New York 14853-1301

Received: April 28, 2003; In Final Form: June 20, 2003

$^{15}\text{N}$  CSA– $^{15}\text{N}$ – $^1\text{H}$  dipolar cross-correlation ( $\eta_{xy}$ ) in proteins has been treated thus far with the model-free (MF) approach, where the global ( $\mathbf{R}^C$ ) and local ( $\mathbf{R}^L$ ) motions are assumed to be decoupled as a consequence of  $\mathbf{R}^L \gg \mathbf{R}^C$ . In the context of  $\eta_{xy}$ , it is additionally assumed that the local motion is very fast and highly symmetrical. We have recently applied to auto-correlated  $^{15}\text{N}$  spin relaxation the slowly relaxing local structure (SRLS) approach, which accounts rigorously for mode-coupling. SRLS can analyze  $\eta_{xy}$  for arbitrary time scale separations between  $\mathbf{R}^L$  and  $\mathbf{R}^C$ . Simulations of  $\eta_{xy}$  for slow local motions are presented herein for the first time. Experimental  $\eta_{xy}$  values of RNase and AKeco could not be reproduced from best-fit parameters generated by data fitting that used axial potentials. Calculations showed they are reproducible using rhombic coupling/ordering potentials. The conformational exchange term,  $R_{ex}$ , “absorbs” potential rhombicity when axial potentials are used to fit the data.  $^{15}\text{N}$  CSA variability and  $\mathbf{R}^C$  anisotropy are shown to have a small effect on the analysis. The shape of the rhombic potentials detected corresponds to nearly “planar  $Y_M X_M$  ordering” (M denotes the local ordering frame). This potential form is consistent with the known geometry of the peptide plane, the SRLS dynamic model in the  $\mathbf{R}_\perp^L \approx \mathbf{R}^C$  regime, and makes possible associating the local director with the  $C_{i-1}^\alpha - C_i^\alpha$  axis. It is shown that back-calculation of NMR variables from the best-fit parameters and comparison with the experimental counterparts is an effective tool for identifying inappropriate elements of the dynamic model and can thereby help improve it.

## Introduction

The ability to interpret nuclear spin relaxation properties in terms of microdynamic parameters turned NMR into a powerful method for elucidating protein dynamics.<sup>1,2</sup> The amide  $^{15}\text{N}$  spin in proteins is a particularly useful probe, relaxed predominantly by dipolar coupling to the amide proton and  $^{15}\text{N}$  chemical shift anisotropy (CSA).<sup>3</sup> The experimental NMR observables are controlled by the global and local dynamic processes experienced by protein N–H bond vectors, which determine the spectral density function,  $J(\omega)$ .  $^{15}\text{N}$  relaxation data in proteins are commonly analyzed with the original and extended versions of the model-free (MF) approach, which assume that the global and local motions are decoupled.<sup>4–6</sup>

In a recent study,<sup>7</sup> we applied the two-body slowly relaxing local structure (SRLS) approach developed by Freed and co-workers<sup>8,9</sup> to auto-correlated  $^{15}\text{N}$  relaxation in proteins. SRLS accounts rigorously for dynamical coupling between the local and global motions. It treats the global diffusion ( $\mathbf{R}^C$ ), the local diffusion ( $\mathbf{R}^L$ ), the local ordering ( $\mathbf{S}$ ) associated with the coupling potential, and the magnetic interactions as asymmetric tensors of arbitrary orientation, providing thereby important information related to protein structure.<sup>10–12</sup> Previous studies<sup>7,13,14</sup> indicated that currently available experimental auto-correlated  $^{15}\text{N}$  relaxation data are sensitive to the SRLS

enhancements, with the dynamic picture provided by SRLS significantly more accurate, physically informative, and discriminating than the dynamic picture provided by MF.

In this study, we apply SRLS to  $^{15}\text{N}$  CSA– $^{15}\text{N}$ – $^1\text{H}$  dipolar cross-correlated relaxation.<sup>15</sup> Experimental methods for measuring  $^{15}\text{N}$ -related cross-correlated relaxation rates were developed recently.<sup>16,17</sup> In the context of proteins this phenomenon was treated thus far exclusively with an MF-based approach.<sup>16</sup> For an axial  $^{15}\text{N}$  CSA tensor with principal axis nearly collinear with the N–H bond one has  $J^{\text{dd}}(\omega) \approx J^{\text{cc}}(\omega)$ , where  $J^{\text{dd}}(\omega)$  and  $J^{\text{cc}}(\omega)$  denote, respectively, the dipolar auto-correlation and CSA auto-correlation spectral densities. For isotropic global diffusion and very fast and highly symmetrical local motions,  $J^{\text{dd}}(\omega) = J^{\text{cd}}(\omega)/P_2(\cos \theta)$ , where  $J^{\text{cd}}$  denotes the cross-correlated spectral density,  $P_2$  is the associated Legendre polynomial of rank 2, and  $\theta$  is the tilt angle between the principal axes of the  $^{15}\text{N}$  CSA and dipolar  $^{15}\text{N}$ – $^1\text{H}$  tensors.<sup>16</sup> The transverse cross-correlated relaxation rate,  $\eta_{xy}$ , is then given for small  $\theta$  by  $\eta_{xy} = 2\alpha d[4J^{\text{dd}}(0) + 3J^{\text{dd}}(\omega_N)]P_2(\cos \theta)$ , where  $d = \gamma_H^2 \gamma_N^2 \hbar^2 / (80\pi^2 r_{\text{HN}}^6)$  and  $\alpha = -4\pi/3 B_0(\sigma_{\parallel} - \sigma_{\perp})r_{\text{HN}}^3 / (\hbar \gamma_H)$ , with the various constants having their usual connotation.<sup>16</sup> With the assumptions outlined above, the spectral density term in this formula is practically identical with the spectral density term in the expression for  $1/T_2$ .<sup>18</sup> This renders the dynamic information content of  $\eta_{xy}$  redundant. However, the expressions for  $\eta_{xy}$  and  $1/T_2$  differ in the coefficients multiplying the term  $[4J^{\text{dd}}(0) + 3J^{\text{dd}}(\omega_N)]$ , with the product  $(\eta_{xy}) \times (T_2)$  depending on  $(\sigma_{\parallel} - \sigma_{\perp})$  and  $\theta$ . Therefore,  $\eta_{xy}$  has been used primarily within the scope of the product  $(\eta_{xy}) \times (T_2)$  to extract information on  $^{15}\text{N}$  CSA variations in “rigid” (i.e., experiencing fast local motion)

\* To whom correspondence should be addressed. (E.M.) E-mail: eva@nmrsgil.lsbu.ac.il. Phone: 972-3-5318049. Fax: 972-3-5351824. (J.H.F.) E-mail: jhf@ccmr.cornell.edu. Phone: 607-255-3647. Fax: 607-255-0595.

<sup>†</sup> Bar-Ilan University.

<sup>‡</sup> Present address: Department of Medical Genetics and Microbiology, Faculty of Medicine, University of Toronto, Toronto, Ontario, Canada.

<sup>§</sup> Cornell University.

protein chain segments. Methods of analysis for determining variations in  $^{15}\text{N}$  CSA,<sup>17–19</sup> identifying conformational exchange terms,  $R_{\text{ex}}$ ,<sup>18</sup> and differentiating between  $R_{\text{ex}}$  contributions and effects associated with global diffusion anisotropy<sup>17</sup> were developed. Assuming validity of the reduced spectral density approach and fast two-site conformational exchange, variants of the common methods of analysis were suggested.<sup>20,21</sup>

These are noteworthy developments, which however involve simplifying assumptions with regard to the nature of the local motion. It is of interest to determine the range of validity of the various MF functionalities mentioned above by comparing SRLS and MF analyses. It was found that MF calculations of  $\eta_{xy}$  and  $(\eta_{xy}) \times (T_2)$  are accurate in the original MF regime within experimental error. This is implied by both  $T_2$  and  $\eta_{xy}$  being given in this parameter range to a large extent by  $J(0)$ , which is dominated by the global motion term. Although the ability to provide information on the local diffusion tensor is therefore limited,  $T_2$  and  $\eta_{xy}$  are expected to be particularly sensitive to the nature of the local ordering tensor,  $\mathbf{S}$ .

This expectation was borne out by the SRLS analysis of the experimental  $^{15}\text{N}$  relaxation data of *E. coli* Ribonuclease H (RNase) and *E. coli* adenylate kinase (AKeco). The main observation made in this study is the combination of (a)  $1/T_2$  and  $\eta_{xy}$  featuring similar experimental profiles, (b) the fact that  $1/T_2$  can, whereas  $\eta_{xy}$  cannot, be reproduced (“back-calculated”) from best-fit parameters obtained using axial potentials, and (c) the fact that best-fit  $R_{\text{ex}}$  on one hand, and experimental  $1/T_2$  and  $\eta_{xy}$  on the other hand, feature similar profiles. This is interpreted in terms of the rhombic symmetry of the local coupling/ordering potential,  $U/k_{\text{B}}T$ , or the asymmetry of the local ordering tensor,  $\mathbf{S}$ , being not accounted for in the fitting scheme for SRLS. Rhombic potentials could be detected using the back-calculation technique due to  $\eta_{xy}$  being independent of  $R_{\text{ex}}$ , whereas the experimental  $1/T_2$  values depend on  $R_{\text{ex}}$ . Experimental evidence, calculations, and general arguments indicate that  $\mathbf{R}^{\text{C}}$  anisotropy and  $^{15}\text{N}$  CSA variability are small effects and can be neglected in the current analysis. Based on experimental data and theoretical SRLS calculations the form of the rhombic coupling potentials prevailing at the N–H bond is determined to correspond to nearly planar  $Y_{\text{M}}X_{\text{M}}$  ordering, with M denoting the local ordering/local diffusion frame.

Several comments on the nature and physical meaning of the SRLS coupling potential,  $U/k_{\text{B}}T(\Omega_{\text{MC}})$ , are in order. The slowly relaxing local structure model expresses the dynamic coupling between a rotationally reorienting particle (body 1), which typically relaxes at a faster rate,  $\mathbf{R}^{\text{L}}$ , and its “local structure” (body 2), which typically relaxes at a slower rate,  $\mathbf{R}^{\text{C}}$ .<sup>8,9</sup> Initially, this was a spin probe in a solvent “cage” but was then adapted to spin-labeled proteins.<sup>10</sup> The coupling materializes through a potential  $U/k_{\text{B}}T(\Omega_{\text{MC}})$  exerted by body 2 at body 1. M denotes the ordering/diffusion frame of body 1, and C denotes the diffusion frame of body 2.  $U/k_{\text{B}}T$  is expanded in the complete basis set of the Wigner rotation matrix elements.<sup>8,9</sup> If only lowest order, i.e.,  $L = 2$ , terms are preserved, the rhombic potential given by  $U/k_{\text{B}}T = -c_0^2 D_{00}^2(\Omega_{\text{CM}}) - c_2^2 [D_{02}^2(\Omega_{\text{CM}}) + D_{0-2}^2(\Omega_{\text{CM}})]$  will be obtained. Assuming axial symmetry, one obtains  $U/k_{\text{B}}T = -c_0^2 D_{00}^2(\Omega_{\text{CM}})$  and a tensor,  $\mathbf{S}$ , featuring a single eigenvalue,  $S_0^2 = S_{zz}$  (with  $S_{xx} = S_{yy} = -S_{zz}/2$ ). The MF analogue of  $S_0^2$  is the generalized order parameter,  $S_s$ .

In the application of SRLS to protein NMR body 1 represents the N–H bond and body 2 the protein. The local coupling or orienting potential represents the spatial restrictions imposed by the protein’s structural features at the site of the local motion of the N–H bond. This is the feature of the model which derives

from the physical attachment of the N–H bond at a specific site in the protein.  $U/k_{\text{B}}T$  constitutes an important site-specific constraint on the reorientational dynamics. By virtue of imposing orientational restrictions on the N–H bond in the protein resulting from the immediate protein surroundings, the potential  $U/k_{\text{B}}T$  couples the local motion of the N–H bond and the global motion of the protein. In the mode-decoupled limit, the time correlation function,  $C(t)$ , contains two terms corresponding to the global and local motion. The global mode is associated with the correlation time  $1/6\mathbf{R}^{\text{C}}$  and its weight in the spectral density is  $(S_0^2)^2$ . The local mode is associated with the correlation time  $1/6\mathbf{R}^{\text{L}}$  and its weight in the spectral density is  $1 - (S_0^2)^2$ . Mode-coupling means that  $C(t)$  comprises additional mixed modes with weights which are functions of the principal values of the tensors  $\mathbf{R}^{\text{C}}$  and  $\mathbf{R}^{\text{L}}$  and the coefficients that define the coupling potential. Mode-decoupling requires the fulfillment of two conditions: large time scale separation between  $\mathbf{R}^{\text{C}}$  and  $\mathbf{R}^{\text{L}}$  and small coupling/orienting potential.

Although in the context of  $\eta_{xy}$  this study focuses largely on the fast local motion regime, we also provide illustrative simulations of  $\eta_{xy}$  in the slow local motion regime. Among other options the ability to calculate accurately  $T_2$  and  $\eta_{xy}$  for slow local motions and rhombic potentials makes possible the general calculation of TROSY<sup>22,23</sup> data.

In summary, this is the first time a method of analysis applicable to cross-correlated relaxation in protein chain segments experiencing slow local motions, which are typically involved in biological function, is offered. Implications to the extensive  $^{13}\text{C}$ -related cross-correlated relaxation data available are particularly important. Also, this is the first report indicating that experimental  $^{15}\text{N}$  spin relaxation data can provide information on physically well-defined rhombic local ordering potentials at each N–H site. Their shape was determined to correspond to nearly planar  $Y_{\text{M}}X_{\text{M}}$  ordering, implicating the  $\text{C}_{i-1}^{\alpha} - \text{C}_i^{\alpha}$  axis as the local director. The conformational exchange term,  $R_{\text{ex}}$ , absorbs potential rhombicity when axial potentials are used to fit the data. A new data analysis tool whereby best-fit NMR variables are back-calculated from the best-fit parameters, and compared with their experimental counterparts, was devised. Back-calculation is an effective tool for identifying inappropriate elements of the dynamic model and can thereby help improve it.

## Theoretical Background

**$\eta_{xy}$  in the Model-Free Approach.** It is assumed that the global and local motions are uncorrelated, the global diffusion is isotropic, the  $^{15}\text{N}$  CSA tensor is axially symmetric with its principal axis tilted at a small angle,  $\theta$ , from the  $^{15}\text{N}$ - $^1\text{H}$  dipolar frame, and the local motions are very fast. In this case, the spectral densities  $J^{\text{dd}}(\omega)$ ,  $J^{\text{cc}}(\omega)$ , and  $J^{\text{cd}}(\omega)$  for dipolar auto-correlation, CSA auto-correlation and dipolar-CSA cross-correlation, respectively, are related as

$$J^{\text{dd}}(\omega) = J^{\text{cc}}(\omega) = J^{\text{cd}}(\omega)/P_2(\cos \theta) \quad (1)$$

The expression for the cross-correlated relaxation rate,  $\eta_{xy}$ , is given by

$$\eta_{xy} = 2\alpha d[4J^{\text{dd}}(0) + 3J^{\text{dd}}(\omega_{\text{N}})]P_2(\cos \theta) \quad (2)$$

where  $d = \gamma_{\text{H}}^2 \gamma_{\text{N}}^2 \hbar^2 / (80\pi^2 r_{\text{HN}}^6)$  and  $\alpha = -4\pi/3B_0(\sigma_{\parallel} - \sigma_{\perp}) - r_{\text{HN}}^3 / (\hbar \gamma_{\text{H}})$ .<sup>16</sup> Corrections for axial global diffusion in the absence of local motions were introduced recently,<sup>24</sup> and applications to  $^{13}\text{C}$ -related cross-correlated relaxation were also pursued.<sup>25–27</sup>

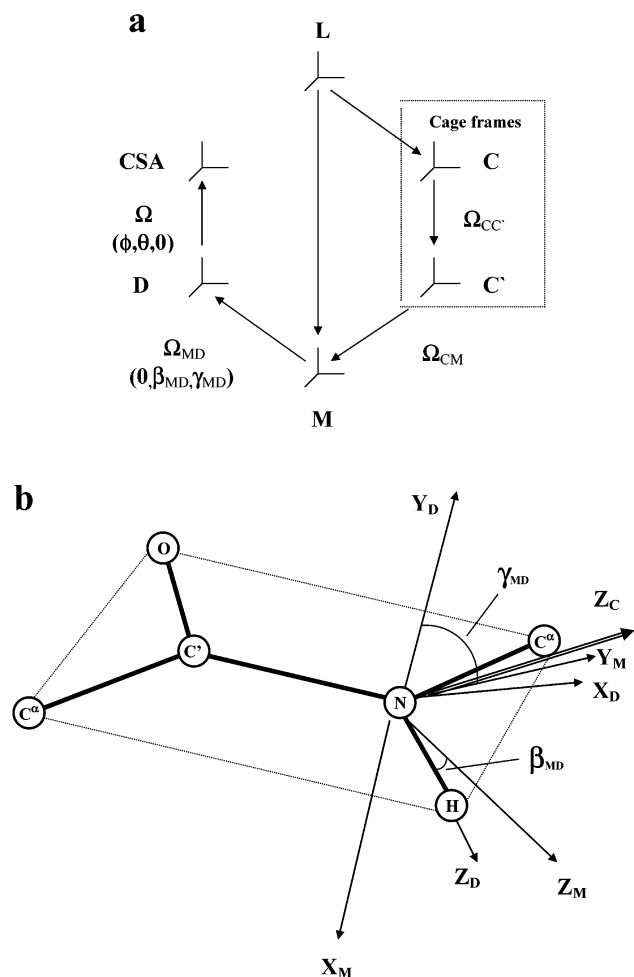


**Figure 1.** (a) Schematic representation of the coordinate frames used in SRLS as applied to N–H bond vector dynamics: L, laboratory frame; C, global diffusion frame; C', local director frame; M, local ordering/local diffusion frame; D, magnetic  $^{15}\text{N}$ - $^1\text{H}$  dipolar tensor frame; CSA, magnetic  $^{15}\text{N}$  CSA tensor frame. For isotropic global diffusion, C and C' are the same. (b) Schematic representation of the geometry in the vicinity of the N–H bond vector.  $X_D$ ,  $Y_D$ , and  $Z_D$  denote the dipolar frame with  $Z_D$  along the N–H bond and  $Y_D$  perpendicular to the peptide plane.<sup>7</sup>  $X_M$ ,  $Y_M$ , and  $Z_M$  denote the local ordering/local diffusion frame. The D  $\rightarrow$  M transformation consists of a rotation  $\beta_{MD}$  about  $Y_D$  followed by a rotation  $\gamma_{MD}$  about the new  $Z_D$  (i.e.,  $Z_M$ ) orientation. The main axis of the local director frame,  $Z_C$ , is depicted close to the N– $\text{C}^\alpha$  bond.

**$\eta_{xy}$  in the SRLS Approach.** SRLS is an effective two-body model for which a Smoluchowski equation representing the rotational diffusion of two interacting rotors is solved. It treats the global diffusion, the local diffusion, the local ordering, and the magnetic interactions as asymmetric tensors of arbitrary orientation. The basics of SRLS in the context of auto-correlated  $^{15}\text{N}$ -related NMR spin relaxation in proteins were outlined previously.<sup>7</sup> The coordinate frames required to describe the SRLS model are depicted in Figure 1a, and the geometry in the vicinity of the N–H bond is depicted in Figure 1b. The laboratory frame, L, is a space-fixed frame with its  $z$  axis along the applied magnetic field. D is the magnetic dipolar tensor frame with  $Z_D$  along the N–H bond and  $Y_D$  perpendicular to the peptide plane.<sup>7</sup> The  $z$  axis of the  $^{15}\text{N}$  CSA tensor (not shown in Figure 1b) is tilted at an angle  $\theta \approx -16^\circ$  (ref 19) from  $Z_D$ , and  $Y_{\text{CSA}}$  is parallel to  $Y_D$ .<sup>7</sup> The Euler angles  $\Omega_{LD}$  and  $\Omega_{\text{LCSA}}$  are the usual stochastic variables of magnetic resonance spin relaxation, modulated by the local motion of the N–H bond vector and the global molecular tumbling. The local potential is related to the orientation of the principal axes of the local

ordering frame, M, with respect to the local director (main C' axis). It is assumed in SRLS that the local diffusion is diagonal in the M frame, which is therefore also related to the internal motion of the N–H bond vector. In general, the D frame is tilted relative to the M frame by Euler angles  $\Omega_{MD}$  ( $\alpha_{MD}$ ,  $\beta_{MD}$ ,  $\gamma_{MD}$ ); since the D frame is axially symmetric,  $\alpha_{MD} = 0$ . C represents the (axial) global diffusion frame and C' the (uniaxial) local director or tilted cage frame,<sup>7–9</sup> with  $\beta_{CC'}$  denoting the angle between  $Z_C$  and  $Z_{C'}$ . For isotropic global diffusion, assumed in this study, the frames C and C' are the same. The main C axis is depicted in Figure 1b to lie close to the  $\text{C}_{i-1}^\alpha - \text{C}_i^\alpha$  axis or the N– $\text{C}_i^\alpha$  bond (see below). The local director may be biaxial, but this property is not accounted for to avoid excessive complexity.<sup>9</sup>

Fundamental equations are given below for convenience. Although only axial ordering potentials were used in previous studies,<sup>7,13,14</sup> in this work, we use asymmetric potentials given by<sup>9,10</sup>

$$U(\Omega_{CM})/k_B T = -c_0^2 D_{00}^2(\Omega_{CM}) - c_2^2 [D_{02}^2(\Omega_{CM}) + D_{0-2}^2(\Omega_{CM})] \quad (3)$$

with C denoting the global diffusion frame and M the coinciding local ordering and local diffusion frames.<sup>7–9</sup> The order parameters associated with the ordering tensor, S, are

$$S_0^2 = \langle D_{00}^2[\Omega_{CM}(t)] \rangle \quad (4)$$

and

$$S_2^2 = \langle D_{02}^2[\Omega_{CM}(t)] + D_{0-2}^2[\Omega_{CM}(t)] \rangle \quad (5)$$

The ensemble averages are defined in terms of the orienting potential in eq 3

$$\langle D_{0n}^2[\Omega_{CM}(t)] \rangle = \int d\Omega D_{0n}^2(\Omega) \exp[-c_0^2 D_{00}^2(\Omega) - 2c_2^2 \text{Re} D_{02}^2(\Omega)] / \int d\Omega \exp[-c_0^2 D_{00}^2(\Omega) - 2c_2^2 \text{Re} D_{02}^2(\Omega)] \quad (6)$$

Axial potentials<sup>7,13,14</sup> feature only the first term of eq 3 and  $S_2^2 = 0$ .

The solution of the Smoluchowski equation features three distinct eigenvalues (correlation times) for axial local motion when the ordering potential is zero

$$(\tau_K)^{-1} = 6\mathbf{R}_\perp^L + K^2(\mathbf{R}_\parallel^L - \mathbf{R}_\perp^L) \text{ for } K = 0, 1, 2 \quad (7)$$

where  $\mathbf{R}_\parallel^L = 1/(6\tau_\parallel)$  and  $\mathbf{R}_\perp^L = 1/(6\tau_\perp) = 1/(6\tau_0)$ . Each K value leads to its own spectral density component  $j_{K=0}(\omega)$ ,  $j_{K=1}(\omega)$ , and  $j_{K=2}(\omega)$ .<sup>28</sup> In the general case, the solution consists of eigenvalues  $1/\tau(i)$  and weighing factors  $c_K(i)$  such that

$$j_K(\omega) = \sum_i c_K(i) \tau(i) / (1 + \omega^2 \tau(i)^2) \quad (8)$$

The eigenvalues  $1/\tau(i)$  represent pure or mixed dynamic modes, in accordance with the parameter range considered. The SRLS function  $J(\omega)$  is constructed out of the  $j_K(\omega)$  components according to<sup>28</sup>

$$J_{\mu\nu}(\omega) = \sum_{K,K'} F_\mu^{2,K} F_\nu^{2,K'} j_{K,K'}(\omega) \quad (9)$$

F denotes the irreducible magnetic tensor components that multiply the spin operators in the spin Hamiltonian,<sup>29</sup> and K



denotes the quantum number associated with the local ordering tensor,  $\mathbf{S}$ , and the local diffusion tensor,  $\mathbf{R}^L$ , given in eq 7. The index  $\mu$  denotes the  $^{15}\text{N}$  CSA interaction diagonal in the CSA ( $'$ ) frame, and  $\nu$  the  $^{15}\text{N}$ - $^1\text{H}$  dipolar interaction diagonal in the DD ( $''$ ) frame.<sup>7</sup> The frames DD and CSA coincide in eq 9. If they are tilted an additional transformation from the CSA to the DD frame, with Euler angles  $\Theta = (0^\circ, \theta^\circ, 0^\circ)$  for an axial  $^{15}\text{N}$  CSA tensor and  $\Theta = (\phi^\circ, \theta^\circ, 0^\circ)$  for an asymmetric  $^{15}\text{N}$  CSA tensor, is required. The Euler angles for the DD to M transformation, implied by eq 9, are  $\Theta = (0^\circ, \beta_{\text{MD}}^\circ, \gamma_{\text{MD}}^\circ)$ . The frame transformations are carried out according to<sup>28</sup>

$$F_{\mu,j}^{2,K} = \sum_{K'} D_{K',K}^2(\Theta) F_{\mu,j}^{2,K'} \quad (10)$$

Concise expressions for the SRLS spectral density for dipolar auto-correlation,  $J^{\text{dd}}(\omega)$ ,  $^{15}\text{N}$  CSA auto-correlation,  $J^{\text{cc}}(\omega)$ , and  $^{15}\text{N}$  CSA- $^{15}\text{N}$ - $^1\text{H}$  dipolar cross-correlation,  $J^{\text{cd}}(\omega)$ , are

$$J^x(\omega) = A(x)j_{K=0}(\omega) + B(x)j_{K=1}(\omega) + C(x)j_{K=2}(\omega) \quad (11)$$

where the coefficients  $A(x)$ ,  $B(x)$ , and  $C(x)$ , with  $x$  denoting cc, dd or cd, feature the trigonometric expressions obtained by the frame transformations. The measurable relaxation quantities are calculated as a function of  $J(0)$ ,  $J(\omega_{\text{N}})$ ,  $J(\omega_{\text{H}})$ ,  $J(\omega_{\text{H}} + \omega_{\text{N}})$ , and  $J(\omega_{\text{H}} - \omega_{\text{N}})$  using standard expressions for NMR spin relaxation,<sup>3,30</sup> where  $J(\omega)$  is obtained from  $J^x(\omega)$  by incorporating the magnetic interactions. Note that the spectral densities  $j_K(\omega)$  are the building blocks for a given dynamic model, whereas the spectral densities  $J^x(\omega)$  are the building blocks for a specific geometric implementation of this dynamic model. If the  $^{15}\text{N}$  CSA tensor is asymmetric  $J^{\text{cc}}(\omega)$  and  $J^{\text{cd}}(\omega)$  also feature rhombic components (eq 10).

The SRLS expression for  $\eta_{xy}$  is given by<sup>15</sup>

$$\eta_{xy} = 2\alpha d[4J^{\text{cd}}(0) + 3J^{\text{cd}}(\omega_{\text{N}})] \quad (12)$$

with  $\alpha$  and  $d$  as in eq 2 and  $J^{\text{cd}}(\omega)$  given by eq 11. The global diffusion tensor,  $\mathbf{R}^C$ , was assumed to be isotropic in this study, with  $\mathbf{R}^C = 1/(6\tau_{\text{m}})$ .

## Materials and Methods

**Sample Preparation.** For preparation of uniformly  $^{15}\text{N}$ -labeled AKeco, *E. coli* HB101 cells transformed with the pEAK91 plasmid were grown at 37 °C in Celtone-N medium (Martek Biosciences Corp., U.S.A.) containing >98%  $^{15}\text{N}$ . The recombinant plasmid pEAK91 contained the intact gene coding for *E. coli* adenylate kinase.<sup>31</sup> The previously described procedure for purification of AKeco<sup>32</sup> was improved by application of Blue-Sepharose affinity chromatography,<sup>31</sup> followed by size-exclusion chromatography on a Sephacryl S-100 column (Pharmacia, Sweden). AKeco stock solution was prepared by thorough dialysis of the protein solution against 40 mM sodium-phosphate buffer (pH 6.8) containing 10  $\mu\text{M}$  sodium azide, followed by concentration on a Centricon-10 concentrator (Amicon, U.S.A.). The concentration of the AKeco solution was determined based on the absorption coefficient  $A_{277} = 0.5 \text{ mg/mL}^{-1} \text{ cm}^{-1}$ .<sup>33</sup> The sample contained 1.75 mM  $^{15}\text{N}$ -labeled enzyme and 40 mM sodium phosphate buffer in 95%  $\text{H}_2\text{O}$ /5%  $\text{D}_2\text{O}$ . It was degassed and transferred to a 5 mm NMR Shigemi cell. Protein mono-dispersion was ascertained previously.<sup>34</sup>

**NMR Spectroscopy.** NMR experiments were carried out at 303 K on Bruker DMX-600 and DRX-800 spectrometers

operating at 14.10 and 18.79 T, respectively, using 5 mm  $^1\text{H}$ - $^{13}\text{C}$ - $^{15}\text{N}$  triple resonance inverse detection probes and B-VT-2000 and BTO-2000 temperature control units at 14.10 and 18.79 T, respectively. NMR data were analyzed on Silicon Graphics workstations using the software packages nmrPipe and modelXY.<sup>35</sup> The previously determined assignments of the AKeco  $^1\text{H}$ - $^{15}\text{N}$  correlations,<sup>36</sup> complemented and revised in our earlier study,<sup>34</sup> were used.

Relaxation times  $T_1$  and  $T_2$  and NOE parameters were measured using established inversion recovery,<sup>37</sup> spin-echo,<sup>38</sup> and  $^{15}\text{N}$ - $\{^1\text{H}\}$  steady-state NOE<sup>39</sup> pulse sequences, as described in refs 40–42. A 0.5 ms spin-echo period was used in the CPMG  $T_2$  experiments. For NOE experiments, we used sequence 1B of ref 42, which features  $\text{H}_2\text{O}$  flip-back pulses to minimize saturation of water. The  $^{15}\text{N}$  CSA- $^{15}\text{N}$ - $^1\text{H}$  dipolar cross-correlated relaxation rate  $\eta_{xy}$  was measured using the pulse sequence developed by Tjandra et al.<sup>16</sup> Spectral widths were 1824.5 and 2432.6 Hz in the  $F_1$  dimension and 9615.4 and 12820.5 Hz in the  $F_2$  dimension at 14.10 and 18.79 T, respectively. The  $^{15}\text{N}$  carrier was set at 117.5 ppm and was referenced indirectly to liquid  $\text{NH}_3$ .<sup>43</sup> A total of  $360 \times 2048$  complex points were acquired in the  $t_1 \times t_2$  dimensions for each time point.

The  $^{15}\text{N}$   $T_1$  and  $T_2$  measurements were performed using a total of 40 and 64 transients per  $t_1$  experiment, respectively. For the  $T_1$  measurements of AKeco, nine time points were collected using parametric delays of 15, 127, 247, 367, 487, 647, 807, 1031, and 1287 ms at 14.10 T and 15, 127, 327, 567, 807, 1047, 1367, 1767, and 2247 ms at 18.79 T. The experiment was repeated twice for time-points 15, 487, and 1287 ms at 14.10 T and 15, 807, and 2247 ms at 18.79 T. The delay between scans was set to 1.5 s at 14.10 T and 2 s at 18.79 T. For the  $T_2$  measurements, nine time points were collected using parametric delays of 8, 16, 24, 32, 48, 64, 80, 96, and 128 ms at 14.10 T, and eight time points were collected using parametric delays of 8, 16, 32, 48, 64, 80, 104, and 128 ms at 18.79 T. The experiment was repeated twice for time-points 8, 64, and 128 ms. The delay between scans was set to 1.6 s at 14.10 T and 1.9 s at 18.79 T. The data were apodized with a cosine (cosine-bell) window function in  $t_1$  ( $t_2$ ). Duplicates were used to calculate average values of, and uncertainties in, the measured peak heights. Phenomenological  $T_1$  and  $T_2$  values and uncertainties were determined by nonlinear least-squares fitting of the experimental data to monoexponential equations.<sup>44</sup>

The  $^{15}\text{N}$ - $\{^1\text{H}\}$  NOE values were measured using pairs of spectra recorded in an interleaved mode with and without proton presaturation during the recycle delay. A total of 96 transients per  $t_1$  experiment were recorded. The delay between scans was 3.8 and 6.6 s at 14.10 T and 5.4 s at 18.79 T. The data were processed as described above. The  $^{15}\text{N}$ - $\{^1\text{H}\}$  NOE values were recorded in duplicate, and the replicates were used to determine uncertainties and mean values.

For the  $\eta_{xy}$  measurements, two experiments were performed with (presat) and without (ref) presaturation applied during the dephasing delay  $2\Delta$ .<sup>16</sup> A total of 192 transients per  $t_1$  experiment were collected. The  $2\Delta$  values were chosen so that  $\langle T_2 \rangle / 4 < 2\Delta < \langle T_2 \rangle$ , where  $\langle T_2 \rangle$  represents the average of the in-phase and anti-phase relaxation times.<sup>16</sup> The value of  $2\Delta$  was set at 14, 32, and 54 ms at 14.10 T and 14 and 32 ms at 18.79 T. The time delay between scans was 1.4 s at 14.10 T and 1.8 s at 18.79 T. Duplicate experiments were carried out to estimate uncertainties and mean values with  $2\Delta$  set at 14 and 32 ms for both 14.10 and 18.79 T. The data were apodized with a cosine (squared cosine-bell) window function in  $t_1$  ( $t_2$ ) dimensions.

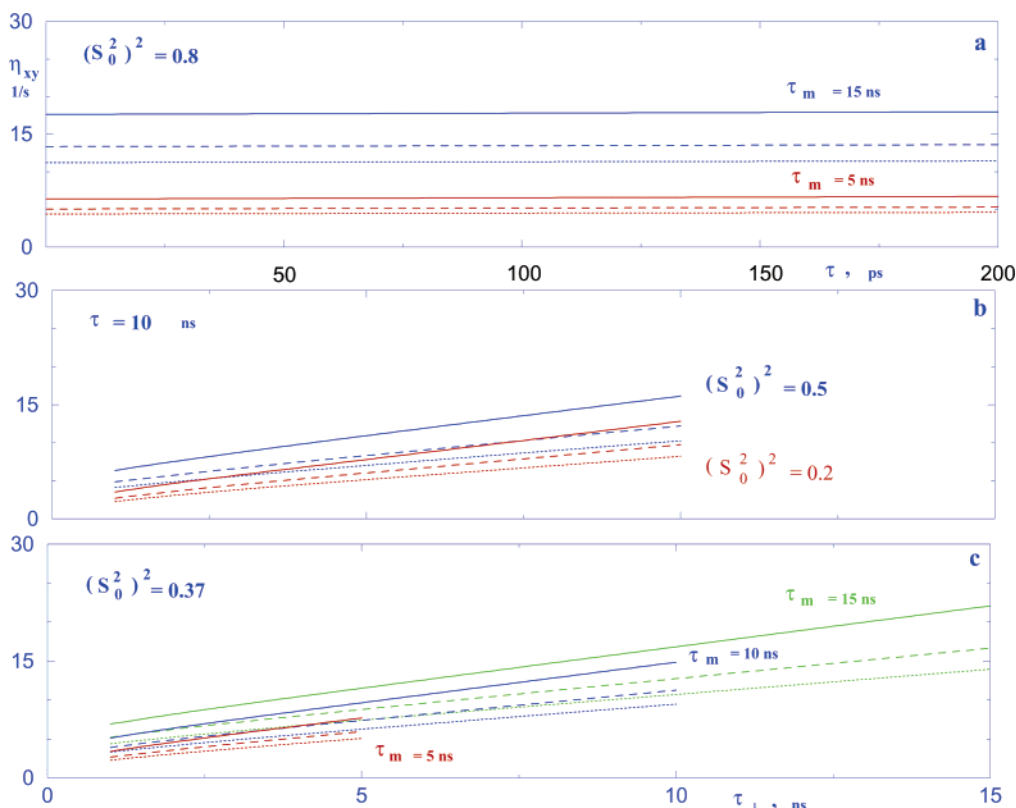


**Figure 2.** Cross-correlated relaxation rate,  $\eta_{xy}$ , as a function of  $\tau$  obtained with  $\mathbf{R}^C/\mathbf{R}^L = 0.0045$ ,  $\tau_m = 15.1$  ns,  $c_0^2 = 9.87$   $k_B T$  [ $(S_0^2)^2 = 0.8$ ] and  $\beta_{MD} = 0^\circ$  for 11.7 T (dotted curves), 14.10 T (dashed curves) and 18.79 T (solid curves), and for  $\tau_m = 15$  ns (upper triplet, blue) and 5 ns (lower triplet, red) (a). Cross-correlated relaxation rate,  $\eta_{xy}$ , as a function of  $\tau_\perp$  obtained with  $\mathbf{R}^C/\mathbf{R}_\perp^L = 0.57$ ,  $\mathbf{R}_\perp^L/\mathbf{R}_\perp^L \rightarrow 0$ ,  $\beta_{MD} = 20^\circ$  and  $\gamma_{MD} = -90^\circ$  for 11.7 T (dotted curves), 14.10 T (dashed curves), and 18.79 T (solid curves).  $\tau_m = 10$  ns and  $c_0^2 = 3.95$   $k_B T$  [ $(S_0^2)^2 = 0.5$ ] (upper triplet, blue), or  $c_0^2 = 2.05$   $k_B T$  [ $(S_0^2)^2 = 0.2$ ] (lower triplet, red) (b).  $c_0^2 = 3$   $k_B T$  [ $(S_0^2)^2 = 0.37$ ] and  $\tau_m = 15$  ns (upper triplet extending up to 15 ns, green), 10 ns (middle triplet extending up to 10 ns, blue), or 5 ns (lower triplet extending up to 5 ns, red) (c).

The cross-correlated relaxation rate  $\eta_{xy}$  was determined for each amino acid residue from the intensity ratio  $I_{\text{presat}}/I_{\text{ref}}$  based on

$$I_{\text{presat}}/I_{\text{ref}} = \tanh(\eta_{xy} 2\Delta) \quad (13)$$

where  $I_{\text{presat}}$  and  $I_{\text{ref}}$  denote the peak intensities in experiments with and without presaturation.<sup>16</sup>

**Data Analysis.** The calculation of SRLS spectral densities is computationally intensive for  $c_{20}$  values exceeding  $\sim 10$  ( $S^2$  exceeding  $\sim 0.81$ ) and/or very fast internal motions. Therefore, in adapting SRLS to protein relaxation analysis, we used precalculated two-dimensional grids of  $j(0)$ ,  $j(\omega_N)$ ,  $j(\omega_H)$ ,  $j(\omega_H + \omega_N)$ , and  $j(\omega_H - \omega_N)$  to fit experimental  $^{15}\text{N}$   $T_1$ ,  $T_2$ , and  $^{15}\text{N}$ - $\{^1\text{H}\}$  NOE data.<sup>7</sup> The  $j_{K=0}$ ,  $j_{K=1}$ , and  $j_{K=2}$  grids of spectral density values at the five frequencies were constructed under the assumption of isotropic global motion for sets of  $c_0^2$  and  $\tau_\parallel$  (or  $\tau_\perp$ ) values. An axial  $^{15}\text{N}$  chemical shielding tensor with  $\sigma_\parallel - \sigma_\perp = -170$  ppm,  $r_{\text{NH}} = 1.02$  Å, and  $\theta = -16^\circ$  (e.g., see ref 19) were used to obtain the  $j(\omega)$  functions. The  $c_0^2$  grid dimension spanned the values between 0 ( $(S_0^2)^2 = 0$ ) and 40  $k_B T$  ( $(S_0^2)^2 = 0.95$ ), and the  $\tau$  dimension spanned the values between  $0.0005\tau_m$  and  $1.4\tau_m$ . The ratio  $\tau/\tau_m$  was interpolated to 0 as required. A two-dimensional polynomial interpolation using Neville's algorithm<sup>45</sup> was employed for spectral density evaluation in the course of model fitting. The interpolation errors in both the  $c_0^2$  and  $\tau$  grid dimensions were estimated to be at least 1 order of magnitude smaller than the errors in the fitted microdynamic parameters. The fitting of experimental NMR data was based on Powell minimization<sup>45</sup> of a target function. The target function for spin  $i$  was defined as the sum of the

squared differences between experimental and calculated  $T_1$ ,  $T_2$ , and  $^{15}\text{N}$ - $\{^1\text{H}\}$  NOE values divided by the squared random errors

$$\chi_i^2 = \sum [(T_{1i}^{\text{obs}} - T_{1i}^{\text{calc}})/\sigma_{T_{1,i}}]^2 + [(T_{2i}^{\text{obs}} - T_{2i}^{\text{calc}})/\sigma_{T_{2,i}}]^2 + [(\text{NOE}_i^{\text{obs}} - \text{NOE}_i^{\text{calc}})/\sigma_{\text{NOE}_i}]^2 \quad (14)$$

where the sum runs over the magnetic fields used in acquiring the experimental data. The model selection scheme employed in the fitting program was based on  $\chi^2$ - and  $F$ -statistic testing and followed closely the schemes used for MF analysis, as described previously.<sup>7</sup> Errors in microdynamic parameters were evaluated based on Monte Carlo simulations<sup>46</sup> using 100 randomly distributed synthetic data sets. Convergence was ascertained by obtaining practically identical results with a larger number of Monte Carlo simulations in representative calculations.

## Results and Discussion

**1. SRLS Simulations of  $\eta_{xy}$ .** Figure 2a illustrates the  $\tau$  dependence of  $\eta_{xy}$  up to 200 ps for  $\tau_m = 5$  and 15 ns and magnetic fields of 11.7–18.79 T. For  $\tau_m = 15$  ns, the cross-correlated relaxation rate  $\eta_{xy}$  increases by approximately 2% for magnetic fields of 11.7–18.79 T within this range. For  $\tau_m = 5$  ns, the analogous increase in  $\eta_{xy}$  is on the order of 5%. Limited  $\tau$  dependence implies validity of eq 2. Extended calculations indicate that eq 2 is valid for  $\tau_m \geq 10$  ns,  $(S_0^2)^2 \geq 0.75$  and  $0 \leq \tau \leq 200$  ps.

The MF-based method (eq 2) is not applicable to calculate  $\eta_{xy}$  generated by residues engaged in slow local motions. Therefore, the SRLS results shown below constitute the first

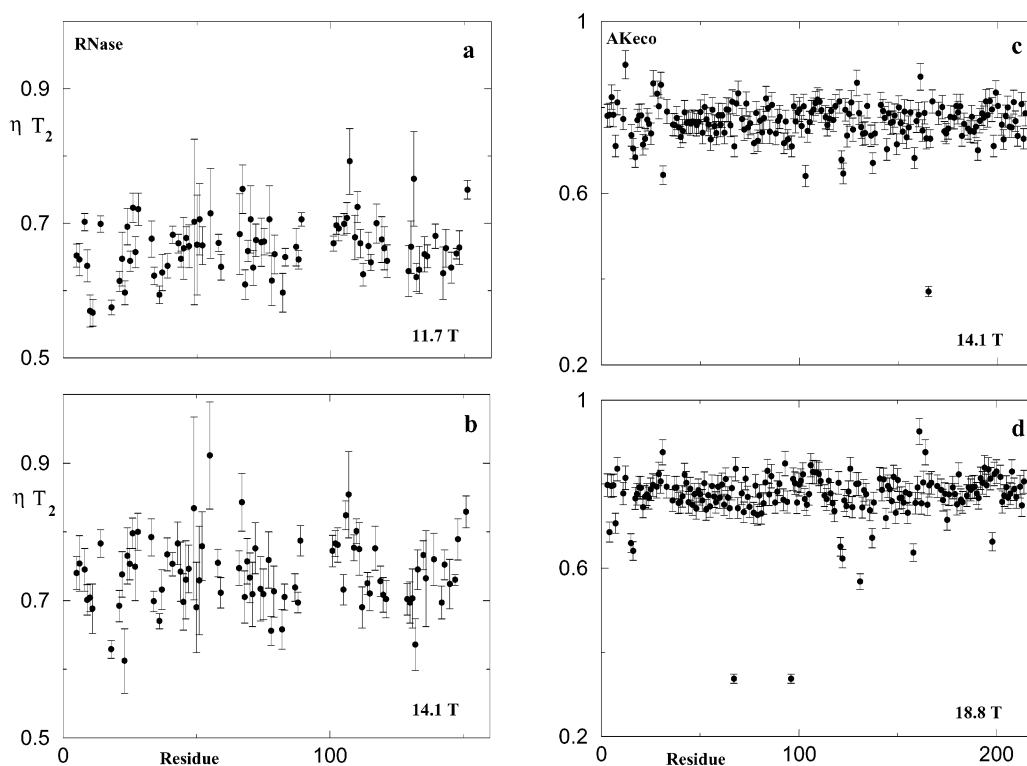


**Figure 3.** Experimental  $(\eta_{xy}) \times (T_2)$  profiles of RNase obtained at 300 K as function of residue number at (a) 11.7 T and (b) 14.10 T. The RNase data used in this and subsequent figures were taken from ref 20. Experimental  $(\eta_{xy}) \times (T_2)$  profiles of AKeco obtained at 303 K as function of residue number at (c) 14.10 T and (d) 18.79 T.

report of theoretical  $\eta_{xy}$  data in the parameter range where  $\mathbf{R}_L^L$  is on the order of  $\mathbf{R}^C$ . Calculations of  $\eta_{xy}$  for  $1 \leq \tau_{\perp} \leq \tau_m$  ns are shown in Figure 2, parts b and c. The dependence of  $\eta_{xy}$  on  $\tau_{\perp}$  as a function of  $(S_0^2)^2$  and magnetic field strength for  $\tau_m = 10$  ns,  $\beta_{MD} = 20^\circ$ , and  $\gamma_{MD} = -90^\circ$  is shown in Figure 2b. The dependence of  $\eta_{xy}$  on  $\tau_{\perp}$  as a function of  $\tau_m$  and magnetic field strength for  $(S_0^2)^2 = 0.37$  [ $c_0^2 = 3.0$  kBT],  $\beta_{MD} = 20^\circ$ , and  $\gamma_{MD} = -90^\circ$  is shown in Figure 2c. The variations in  $\eta_{xy}$  as a function of the microdynamic parameters  $\tau_{\perp}$  and  $(S_0^2)^2$  are significant. Thus, for  $\tau_m = 10$  ns, the relaxation rate  $\eta_{xy}$  increases by 51% for a 2-fold increase in  $\tau_{\perp}$  and by 80% for a 2.5-fold increase in  $(S_0^2)^2$  (Figure 2b).  $\beta_{MD} = 20^\circ$  and  $\gamma_{MD} = -90^\circ$  are typical values determined in previous studies.<sup>13,14</sup>

With the capability to calculate  $\eta_{xy}$  over the entire parameter range relevant for folded proteins, it is of interest to explore new potential usages of this parameter. As shown below, it is possible to devise new applications. In this study the focus is on the  $\mathbf{R}^C \ll \mathbf{R}^L$  regime.

**2. Cross-Correlation in “Rigid” Residues of RNase.** Kroenke et al.<sup>20</sup> used the transverse  $(\eta_{xy})$  and longitudinal  $(\eta_z)$  cross-correlated  $^{15}\text{N}$  CSA– $^{15}\text{N}$ - $^1\text{H}$  relaxation rates and auto-correlated relaxation rates of RNase to study  $^{15}\text{N}$  CSA variations. Experimental data were acquired at magnetic fields of 11.7, 14.10, and 18.79 T. The complete data set was filtered carefully to leave 81 rigid residues for which eq 2 was considered applicable. Figure 3, parts a and b, shows the product  $(\eta_{xy}) \times (T_2)$  as a function of residue number obtained at 11.7 and 14.10 T. The absence of  $R_{ex}$  contributions was ascertained based on criteria set forth in ref 20. On the basis of the various relaxation rates measured, the  $^{15}\text{N}$  CSA variations were found to be statistically insignificant at 11.7 and 14.10 T and unaffected by the small previously determined  $\mathbf{R}^C$  anisotropy.<sup>17,20,47</sup>

**$^{15}\text{N}$  CSA Variability.** The conclusions of Kroenke et al.<sup>20</sup> that  $^{15}\text{N}$  CSA variations do not affect the analysis below 14.1 T are reinforced by examining the  $(\eta_{xy}) \times (T_2)$  profiles of RNase

obtained at 11.7 and 14.1 T, shown in Figure 3, parts a and b. These profiles are nearly unstructured (omitting outliers with unduly large uncertainties) and similar at both fields. Figure 3, parts b and d, shows the  $(\eta_{xy}) \times (T_2)$  profiles of AKeco obtained at 14.1 and 18.8 T. They are practically flat and similar at both fields. The expressions for  $1/T_2$  and  $\eta_{xy}$  comprise a structural coefficient which is  $0.5[d^2 + f(\theta)c^2]$  for  $1/T_2$  and  $cd P_2(\cos \theta)$  for  $\eta_{xy}$ .  $c$ ,  $d$ , and  $\theta$  have their usual connotations (the definitions of ref 18 were used), and  $f(\theta) = J^{cc}(\omega)/J^{dd}(\omega)$ . These coefficients are multiplied by  $4J(0) + 3J(\omega_N)$ , which we confirmed above to be practically the same<sup>18</sup> for  $1/T_2$  and  $\eta_{xy}$  in the case of rigid residues. In MF,  $J^{cc}(\omega)$  and  $J^{dd}(\omega)$  are taken to be the same, i.e.,  $f(\theta) = 1$ . This is a geometric simplification implied by the MF formulas being valid for a single irreducible magnetic tensor component. Hence,  $^{15}\text{N}$  CSA must be axial and collinear with the  $^{15}\text{N}$ - $^1\text{H}$  dipolar tensor. This subject matter is addressed in the next paper in this journal issue (e.g., Figure 1c and Table 3). Independent of whether the correct expression for  $f(\theta)$  is used or  $f(\theta)$  is set equal to 1, the functional dependences of  $\eta_{xy}$  and  $1/T_2$  on  $\theta$  differ, and a significant effect of  $\theta$  variability would manifest as a structured  $(\eta_{xy}) \times (T_2)$  profile, contrary to experimental evidence. The only provision is that variations in  $\theta$  may be fortuitously compensated by variations in  $c$ . We found that the discrepancies between experimental and back-calculated  $\eta_{xy}$  data, which is the observation we wish to explain, are larger at lower magnetic fields than at higher magnetic fields. Hence,  $c$  variability is not likely to be a major factor.

Kroenke et al.<sup>20</sup> demonstrated that for the rigid RNase residues considered by us the variations in the magnitude of the  $^{15}\text{N}$  CSA tensor do not affect the analysis at 14.1 T and below. Using the same methods of analysis, we reached similar conclusions for the AKeco data acquired at 14.1 and 18.8 T (unpublished results). Fushman et al.<sup>19</sup> reported large variations in both  $^{15}\text{N}$  CSA magnitude and orientation in Ubiquitin. Kroenke et al.<sup>20</sup> showed that the variations in the magnitude of

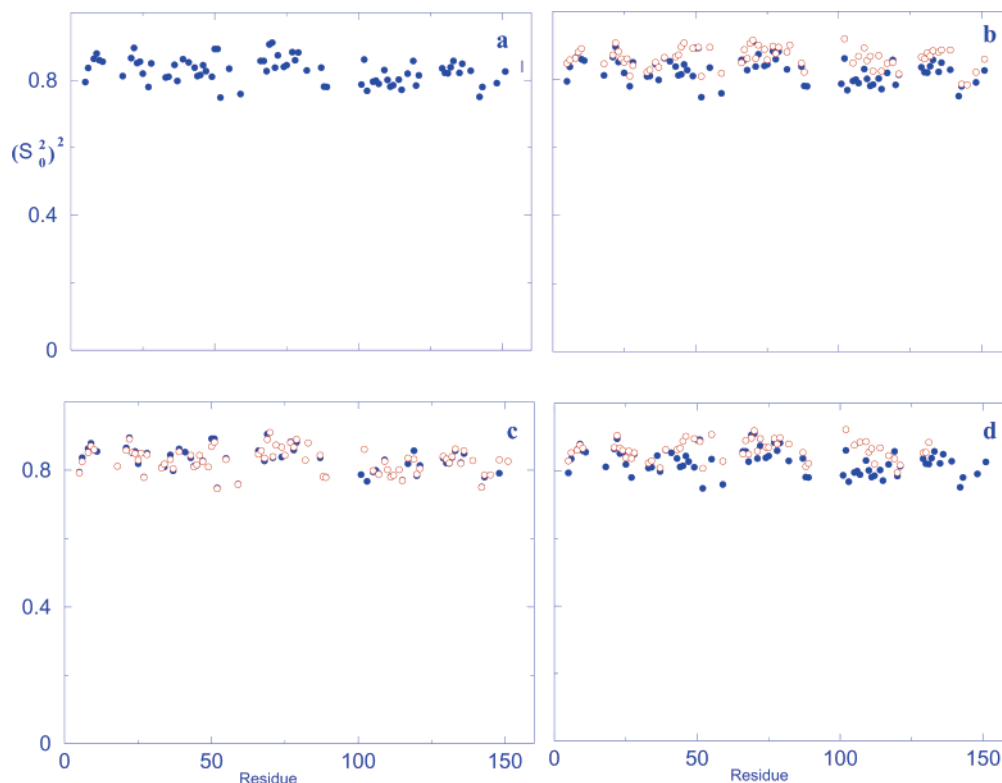


**Figure 4.** Best fit squared order parameter,  $(S_0^2)^2$ , obtained by applying SRLS to the combined 11.7 and 14.1 T data of RNase as a function of residue number, using (a)  $T_1$ ,  $T_2$ , and NOE fitting and  $\tau_m = 9.28$  ns, (b)  $T_1$ ,  $T_2$ , and NOE fitting and site-specific  $\tau_m(i)$  (opaque red circles), (c)  $T_1$ ,  $1/T_2 + \eta_{xy}$ , and NOE fitting and  $\tau_m = 9.28$  ns (opaque red circles), and (d)  $T_1$ ,  $1/T_2 + \eta_{xy}$ , and NOE fitting and site-specific  $\tau_m(i)$  (opaque red circles). The solid blue circles in Figure 4b–d represent Figure 4a data. The experimental RNase data in this and the subsequent figures were taken from ref 20.  $^{15}\text{N}$  CSA of  $\sigma_{\parallel} - \sigma_{\perp} = -170$  ppm,  $r_{\text{NH}} = 1.02$  Å and  $\theta = -16^\circ$  were used in this and subsequent figures. Average error bars are depicted on the right-hand-side of Figure 4a.

the  $^{15}\text{N}$  CSA tensor were overestimated for Ubiquitin because the data set used included several data points with uncertainties much smaller than the remainder of the data. By eliminating these outliers, the distribution in  $^{15}\text{N}$  CSA tensor magnitude became as limited as in RNase. The outlier-based argument is valid for both tensor magnitude and orientation. Hence, the variations in the orientation of the  $^{15}\text{N}$  CSA tensor in Ubiquitin were also overestimated. We are not aware of literature reports on large  $^{15}\text{N}$  CSA tensor variations for rigid residues observed at 14.1 T and below.

Based on this,  $^{15}\text{N}$  CSA tensor variability is not likely to dominate the analysis. Possible effects on the analysis will be considered at the next stage of this work, when absolute values of the rhombic potential coefficients will be determined. At this stage, we focus on dominant effects that explain our observations and the symmetry of the rhombic potential detected.

The analysis outlined above implies that  $\eta_{xy}$  should be reproducible using the best-fit parameters obtained by fitting the auto-correlated relaxation rates. For brevity we denote such data below as reproduced  $\eta_{xy}$  values. Best-fit  $(S_0^2)^2$  and  $R_{\text{ex}}$  profiles obtained with an axially symmetric coupling potential, using combined  $T_1$ ,  $T_2$ , and NOE data of the 81 rigid RNase residues acquired at 11.7 and 14.10 T, are shown in Figures 4a and 5a, respectively. In Figure 6a, we show reproduced  $\eta_{xy}$  values (opaque red circles) superimposed on their experimental counterparts (solid blue circles). Clearly, the prediction regarding  $\eta_{xy}$  reproducibility is not borne out in Figure 6a for a large number of residues. In particular, the experimental  $\eta_{xy}$  values exceed on average by 28% the calculated values in the chain regions 55–59 and 102–107. Note that the largest  $R_{\text{ex}}$  terms in Figure 5a occur in the same chain segments in which Figure 6a shows discrepancies. As already pointed out, the deviations

between reproduced or back-calculated and experimental  $\eta_{xy}$  values were found in to be larger at 11.7 T (not shown) as compared to 14.10 T. A dominant effect implied by variations in the  $^{15}\text{N}$  chemical shift anisotropy is expected to increase at higher fields. Hence, this is an argument against such variability dominating the observed discrepancies.

**$R^{\text{C}}$  Anisotropy.** We investigate below the effect of the small previously detected<sup>17,20,47</sup>  $R^{\text{C}}$  anisotropy. This is accomplished by including  $R^{\text{C}}$  anisotropy and/or  $\eta_{xy}$  data into the RNase data fitting process and using a new approach whereby best-fit NMR variables are back-calculated from the best-fit parameters and compared with their experimental counterparts. Based on the approach of Bruschweiler et al.,<sup>48</sup> which is valid for small  $R^{\text{C}}$  anisotropy, apparent global motion correlations times,  $\tau_m(i)$ , can be associated with each residue  $i$ .  $\tau_m(i)$  values were calculated for each of the 81 rigid RNase residues using the program “quadric”<sup>49</sup> and employed subsequently in SRLS fitting.

The results obtained with the conventional  $^{15}\text{N}$   $T_1$ ,  $T_2$ , and  $^{15}\text{N}\{-^1\text{H}\}$  fitting using, however, residue specific  $\tau_m(i)$  values are shown in Figure 4b, 5b and 6b (opaque red circles). Figure 4b also features the results obtained with constant  $\tau_m$  (solid blue circles), and Figure 6b also features the experimental  $\eta_{xy}$  data (solid blue circles). It can be seen that the  $(S_0^2)^2$  profile changed significantly (Figure 4b), the  $R_{\text{ex}}$  terms were almost totally eliminated (cf. Figures 5a and 5b). However, in general, the discrepancy between the experimental and calculated  $\eta_{xy}$  values remained largely in effect in the chain regions 55–59 and 102–107, and actually increased at the two ends (cf. Figure 6, parts a and b). The NMR variables  $^{15}\text{N}$   $T_1$ ,  $^{15}\text{N}$   $T_2$ , and NOE were back-calculated, and  $\eta_{xy}$  was reproduced using the best-fit parameters for various fitting scenarios. Illustrative results obtained at 14.1 T for residue 55 are shown in Figure 7 (red



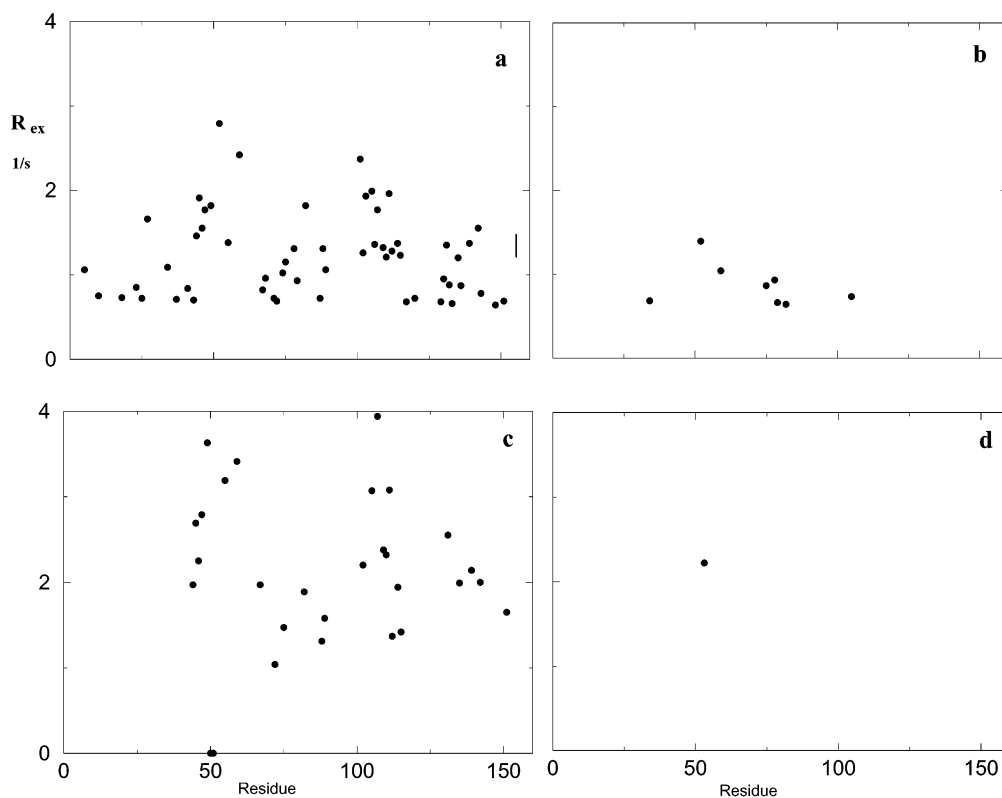


**Figure 5.** Best fit conformational exchange term,  $R_{\text{ex}}$ , obtained by applying SRLS to the combined 11.7 and 14.1 T data of RNase as a function of residue number, using (a)  $T_1$ ,  $T_2$ , and NOE fitting and  $\tau_m = 9.28$  ns, (b)  $T_1$ ,  $T_2$ , and NOE fitting and site-specific  $\tau_m(i)$ , (c)  $T_1$ ,  $1/T_2 + \eta_{xy}$ , and NOE fitting and  $\tau_m = 9.28$  ns, and (d)  $T_1$ ,  $1/T_2 + \eta_{xy}$ , and NOE fitting and site-specific  $\tau_m(i)$ . Average error bars are depicted on the right-hand-side of Figure 5a.

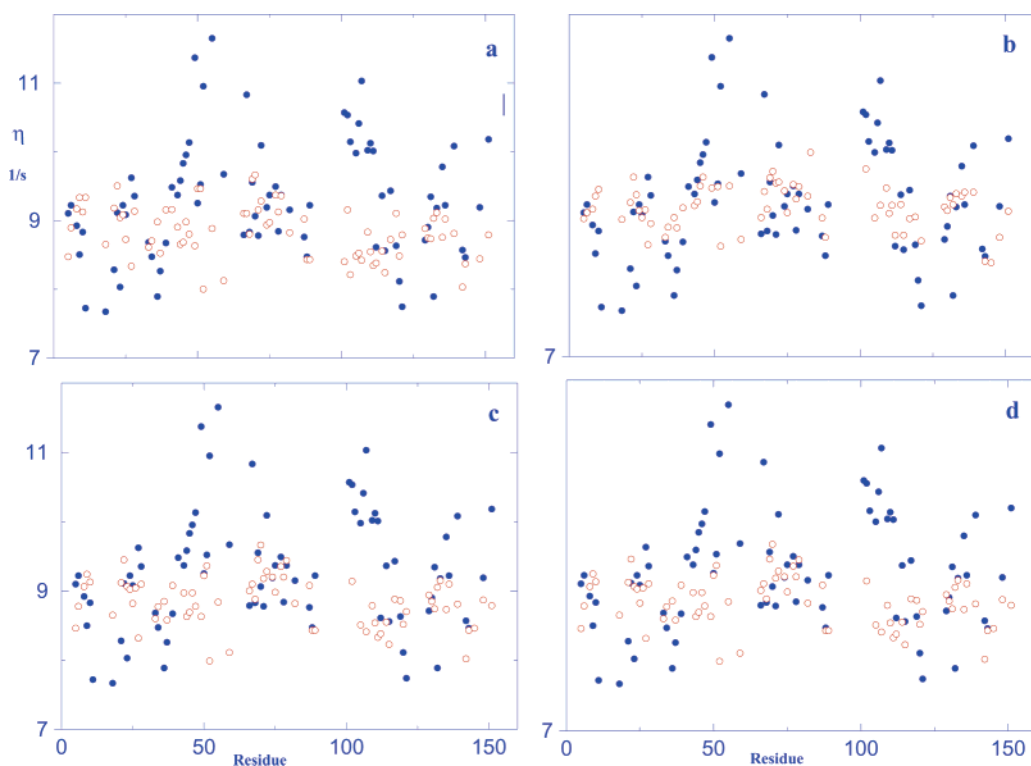


**Figure 6.** Reproduced (Figure 6, parts a and b) and back-calculated (Figure 6, parts c and d) RNase  $\eta_{xy}$  values obtained at 14.1 T as a function of residue number (opaque red circles), using the best-fit parameters corresponding to (a)  $T_1$ ,  $T_2$ , and NOE fitting and  $\tau_m = 9.28$  ns, (b)  $T_1$ ,  $T_2$ , and NOE fitting and site-specific  $\tau_m(i)$ , (c)  $T_1$ ,  $1/T_2 + \eta_{xy}$ , and NOE fitting and  $\tau_m = 9.28$  ns, and (d)  $T_1$ ,  $1/T_2 + \eta_{xy}$ , and NOE fitting and site-specific  $\tau_m(i)$ . The 14.1 T experimental data (solid blue circles) are superimposed in Figure 6a–d. The average error in the experimental data, which is similar to the average error in the calculated data, is depicted on the right-hand-side of Figure 6a.

triangles). The data of interest in the present context include  $T_1$ ,  $T_2$ , and NOE fitting using  $\tau_m(i)$  (red triangles),  $T_1$ ,  $T_2$ , and

NOE fitting using  $\tau_m = 9.28$  ns (solid blue circles), and experimental data (opaque red circles). This triplet is labeled  $\tau$



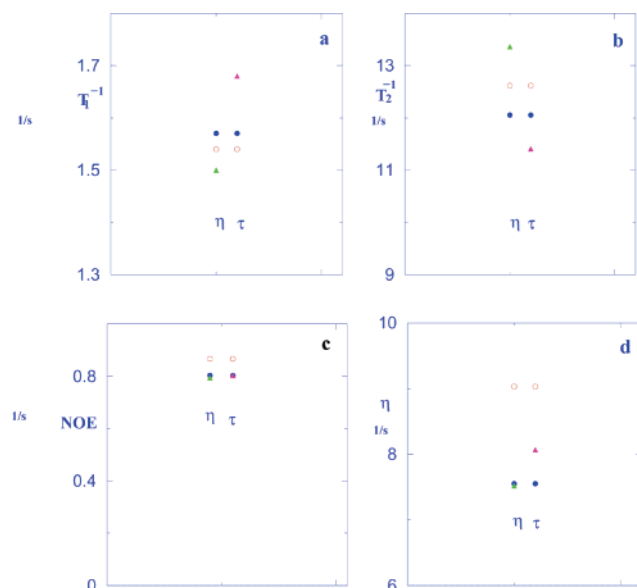


**Figure 7.** 14.1 T experimental (opaque red circles) and back-calculated (a)  $1/T_1$ , (b)  $1/T_2$ , (c) NOE, and (d)  $\eta_{xy}$  (reproduced when not used in fitting) data for residue 55 of RNase. The solid blue circles correspond to  $1/T_1$ ,  $1/T_2$ , and NOE fitting and  $\tau_m = 9.28$  ns. The magenta triangles pertaining to the triplet labeled  $\tau$  correspond to  $1/T_1$ ,  $1/T_2$ , and NOE fitting and variable  $\tau_m(i)$ . The green triangles pertaining to the triplet labeled  $\eta$  correspond to  $1/T_1$ ,  $1/T_2 + \eta_{xy}$ , and NOE fitting and  $\tau_m = 9.28$  ns.

in Figure 7. It can be seen that the quality of  $T_1$  and  $T_2$  fitting was impaired by introducing  $\tau_m(i)$  (Figure 7, parts a and b), entailing an *apparent* improvement in the reproduced 14.1 T  $\eta_{xy}$  value (Figure 7d). If the dynamic model would have been improved genuinely, the correspondence between experimental and back-calculated  $T_1$  and  $T_2$  pairs should have also been improved.

**$T_1$ ,  $1/T_2 + \eta_{xy}$ , and NOE Fitting.** Next we fitted  $T_1$ , the sum  $1/T_2 + \eta_{xy}$ , and the NOE with results presented in Figures 4c, 5c and 6c (opaque red circles). Figure 4c also features the results obtained with constant  $\tau_m$  (solid blue circles), and Figure 6c also features the experimental  $\eta_{xy}$  data (solid blue circles). It can be seen that the  $(S_0^2)^2$  profile did not change (Figure 4c), the small  $R_{ex}$  terms were eliminated but the large  $R_{ex}$  terms in the chain regions 55–59 and 102–107 became even larger (Figure 5c), and the discrepancy between the experimental and calculated  $\eta_{xy}$  values remained practically the same (Figure 6c). In this case, the quality of the 14.1 T  $T_1$  and  $T_2$  fitting was largely preserved, with reversed relative magnitude of theoretical and experimental values (Figure 7, parts a and b, triplets label  $\eta$ ) and practically no change in the reproduced 14.1 T  $\eta_{xy}$  value (Figure 7d, triplet label  $\eta$ ). The last fitting scenario pursued featured  $T_1$ ,  $1/T_2 + \eta_{xy}$ , and NOE as experimental variables and site-specific  $\tau_m(i)$  values. The results are shown in Figures 4d, 5d and 6d (opaque red circles). Figure 4d also features the results obtained with constant  $\tau_m$  (solid blue circles), and Figure 6d also features the experimental  $\eta_{xy}$  data (solid blue circles). These results are very similar to the data shown in Figures 4b, 5b, and 6b.

**Back-Calculation: Force-Fitting.** When inappropriate versions of a given dynamic model are used, force-fitting may set in.<sup>10</sup> This concept refers to the convergence of the target function minimization to statistically acceptable but physically inappropriate minima. Forcing  $\mathbf{R}^C$  anisotropy upon the residue-specific fitting calculations through the utilization of site-specific correlation times,  $\tau_m(i)$ , leads to technical minima that abide

by the statistical criteria but feature microdynamic parameters that differ from the accurate ones. Moreover, the correspondence between input and back-calculated data is worsened. Adding to the fitting process  $\eta_{xy}$ , which as indicated above is dominated in the  $\mathbf{R}^L \gg \mathbf{R}^C$  limit by  $\mathbf{S}$  asymmetry, preserves the quality of the fitting and does not generate force-fitted microdynamic parameters. On the other hand, it generates force-fitted  $R_{ex}$  terms. Back-calculation of best-fit NMR variables and their comparison with the corresponding experimental data is a very useful tool for identifying inappropriate or missing aspects of a given dynamic model and can thereby help improve it.

**Summary.** The results shown in Figure 4c indicate that the spin relaxation information inherent in  $\eta_{xy}$  is, indeed, redundant in the present calculations. As shown in Figure 6, parts a and c, the use of  $\eta_{xy}$  as experimental variable in the fitting process does not improve its own reproduction based on the best-fit parameters. The results shown in Figures 5a,c and 6a,c can be reconciled assuming that  $R_{ex}$  absorbed a physical property inherent in  $\eta_{xy}$ , which has so far not been considered in the SRLS fitting scheme. The experimental value of  $1/T_2$  depends on  $R_{ex}$ , whereas the experimental value of  $\eta_{xy}$  does not depend on  $R_{ex}$ . Therefore, within the scope of data fitting based on axial potentials,  $1/T_2$  is reproduced quite well, whereas  $\eta_{xy}$  is reproduced poorly.

**3. Cross-Correlation in AKeco.** Adenylate kinase from *E. coli* is a three-domain 23.6 kD enzyme which catalyzes the reaction  $\text{ATP} + \text{AMP} = 2 \text{ADP}$ . In solution, the domains AMPbd and LID exhibit extensive catalysis-related mobility.<sup>32,50</sup> On the NMR time scale the molecule prevails in solution as an ensemble of rapidly interconverting conformations.<sup>34</sup> Using axial ordering potentials, it was found previously<sup>13</sup> with SRLS that the structurally preserved domain CORE is relatively rigid, with the N–H bonds engaged in rapid small-amplitude fluctuations. This parameter range, denoted as ps regime, features high parallel  $Z_M$  ordering and  $\mathbf{R}^L \gg \mathbf{R}^C$ .<sup>13,14</sup> The mobile domains AMPbd and LID were shown previously to feature high perpendicular  $Y_M$  ordering.<sup>13,14</sup> The components of the diffusion tensor for local motion are  $\mathbf{R}_{||}^L \gg \mathbf{R}_{\perp}^L$  and  $\mathbf{R}_{\perp}^L \approx \mathbf{R}^C$ , where  $\mathbf{R}_{||}^L$  represents very fast motion about  $Z_M$ , and  $\mathbf{R}_{\perp}^L$  represents slow motion about  $Y_M$ . The orientation of the dipolar frame relative to the local ordering/diffusion frame is given by the Euler angles  $\beta_{MD} \approx 20^\circ$  and  $\gamma_{MD} \approx -90^\circ$ . This was denoted as the ns regime model.<sup>13,14</sup>

The experimental  $(\eta_{xy}) \times (T_2)$  profiles obtained at 14.10 and 18.79 T are shown in Figure 3, parts c and d. The outliers located below the main profile are associated with large  $R_{ex}$  contributions,<sup>18</sup> as pointed out previously<sup>34</sup> for the 14.10 T data. Most of the 14.10 T outliers are also featured by the 18.79 T data. The  $^{15}\text{N}$  CSA variations were found to be statistically insignificant at both 14.10 and 18.79 T using the criteria outlined in ref 20. Both the physical state of this conformationally averaged molecule and previous attempts to determine  $\mathbf{R}^C$  point to an isotropic global diffusion tensor with  $\tau_m = 15.1$  ns.<sup>14,34</sup> As indicated above, the conspicuous flatness of the Figure 3, parts c and d, profiles points to similar dynamic information inherent in  $\eta_{xy}$  and  $1/T_2$ .

**Back-Calculation.** Figure 8a–c shows superimposed best-fit microdynamic parameters obtained for the ps regime of AKeco with  $T_1$ ,  $T_2$ , and NOE fitting (opaque red circles) and  $T_1$ ,  $1/T_2 + \eta_{xy}$ , and NOE fitting (solid blue circles) (similar to RNase, the attempt to replace  $1/T_2$  with  $\eta_{xy}$  turned out problematic). Combined data acquired at 14.10 and 18.79 T were used, and the coupling potential was assumed to be axially symmetric. The  $(S_0^2)^2$  (Figure 8a) and  $\tau$  (Figure 8b) data obtained with the

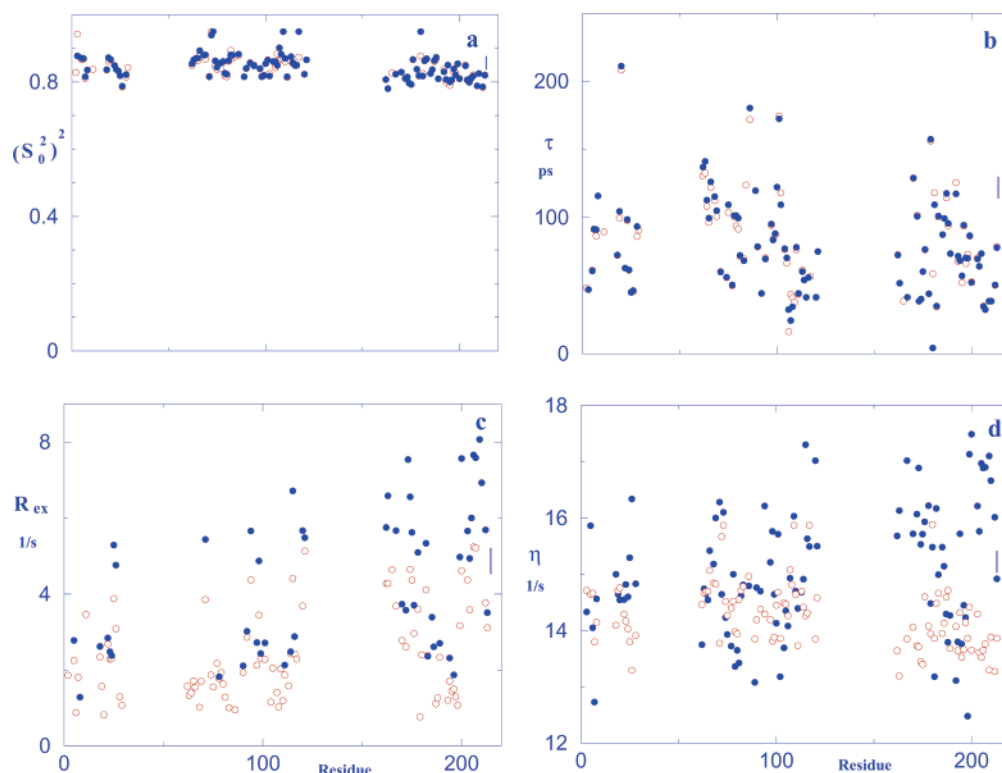


**Figure 8.** Best fit (a) squared order parameter,  $(S_0^2)^2$ , (b) local motion correlation time,  $\tau$ , and (c) conformational exchange term,  $R_{ex}$ , as a function of residue number obtained by applying SRLS to the combined 14.10 and 18.79 T data of the CORE domain of AKeco. The data were generated with  $T_1$ ,  $T_2$ , and NOE fitting (opaque red circles) or  $T_1$ ,  $1/T_2 + \eta_{xy}$ , and NOE fitting (solid blue circles). (d) Back-calculated 14.10 T  $\eta_{xy}$  data obtained with best-fit parameters generated by  $T_1$ ,  $1/T_2 + \eta_{xy}$ , and NOE fitting (opaque red circles), superimposed on the experimental data obtained at 14.10 T (solid blue circles).  $\tau_m = 15.1 \text{ ns}^{13}$  was used in this and subsequent AKeco-related figures. Average error bars for the best-fit parameters (Figure 8a–c) and the experimental  $\eta_{xy}$  data (Figure 8d) are depicted on the right-hand-side of the respective panels.

two fitting scenarios are similar, whereas the  $R_{ex}$  data (Figure 8c) are quite different. In Figure 8d, we show  $\eta_{xy}$  values back-calculated at 14.10 T using the best-fit parameters generated by  $T_1$ ,  $1/T_2 + \eta_{xy}$ , and NOE fitting (opaque red circles), superimposed on the 14.10 T experimental data (solid blue circles). Significant discrepancies between experimental and back-calculated  $\eta_{xy}$  values are observed for many residues, notably the latter part of the chain, where the calculated data underestimate the experimental data on average by 23%. A similar picture (not shown) was obtained for reproduced  $\eta_{xy}$  values calculated using the best-fit parameters generated by  $T_1$ ,  $T_2$ , and NOE fitting. The  $1/T_2$  data provide a different picture. This is illustrated in Figure 9 which presents superimposed experimental and back-calculated  $\eta_{xy}$  data aside superimposed experimental and back-calculated  $1/T_2$  data for the AKeco chain segment Q160–G214. It can be seen that the edge-shaped pattern in the experimental data of both NMR variables (solid blue circles in Figure 9, parts a and b) is mimicked by the best-fit  $R_{ex}$  data (Figure 8c, solid blue circles). Although  $T_2$  fitting turned out successful (Figure 9b),  $\eta_{xy}$  fitting turned out highly inappropriate (Figure 9a). If, as suggested above for RNase, the  $R_{ex}$  terms indeed absorb a physical property unaccounted for in the present calculations, they will help reproduce the experimental  $1/T_2$  data, which depend on  $R_{ex}$ , but not the experimental  $\eta_{xy}$  data, which are independent of  $R_{ex}$ . Thus, the general picture and the implied conclusions are similar for the ps regimes of both proteins.

**Rhombic Potentials.** It is concluded that, for both proteins studied, the  $R_{ex}$  data more properly reflect a physical property, which has not been taken into consideration in the SRLS fitting scheme. As shown below with SRLS calculations, this is potential rhombicity. The evidence against  $^{15}\text{N}$  CSA variability

being the dominant effect was outlined above in the subsection entitled  $^{15}\text{N}$  CSA variability. The evidence against  $\mathbf{R}^C$  anisotropy being the dominant effect is summarized below.

(1) Observed  $\eta_{xy}$  variations are larger at 11.7 T (for RNase) and 14.1 T (for AKeco) than at 18.8 T.  $\mathbf{R}^C$  anisotropy is field-independent.

(2) The global diffusion tensor of AKeco was shown previously to be spherical within a good approximation.<sup>34</sup> The anisotropy of the  $\mathbf{R}^C$  tensor of RNase was shown previously to be small.<sup>17,20,47</sup> We show herein that using for RNase  $\tau_m(i)$  instead on a constant value,  $\tau_m$ , spoils the quality of the fitting instead of improving it, with  $\tau_m(i)$  variations becoming absorbed by the squared order parameter,  $(S_0^2)^2$ .

**4. Shape of the Rhombic Potentials.** We proceed by using SRLS to determine the shape of the rhombic potentials detected. SRLS calculations are currently very tedious for rhombic potentials in the  $\mathbf{R}^L \gg \mathbf{R}^C$  limit. The application of previously developed database pruning capabilities<sup>51</sup> to the protein NMR version of SRLS, which will render these calculations feasible, is underway. Because we aim at determining the symmetry of  $U/k_B T$ , rather than the absolute values of  $c_0^2$  and  $c_2^2$  (eq 3), it is appropriate to resort to the ns regime parameter range which is less demanding computationally. We show below the results of theoretical calculations of  $j_K(\omega)$  (eq 8) and  $J^r(\omega)$  (eq 11), performed using rhombic potentials. The functions  $J^r(\omega)$  depend on the angles  $\theta$ ,  $\beta_{MD}$ , and  $\gamma_{MD}$ , which determine the coefficients  $A(x)$ ,  $B(x)$ , and  $C(x)$  in eq 11. The Wigner rotation from the CSA frame to the DD frame was performed according to eq 10 with  $\Theta = (0^\circ, -16^\circ, 0^\circ)$ .<sup>19</sup> The Wigner rotation from the DD frame to the M frame was performed with  $\Theta = (0, \beta_{MD}, \gamma_{MD})$ . For the ps regime, the assumption that  $\mathbf{R}^L$  is isotropic implies  $\beta_{MD} = 0^\circ$  and independence of the calculation on  $\gamma_{MD}$ .<sup>7</sup> The

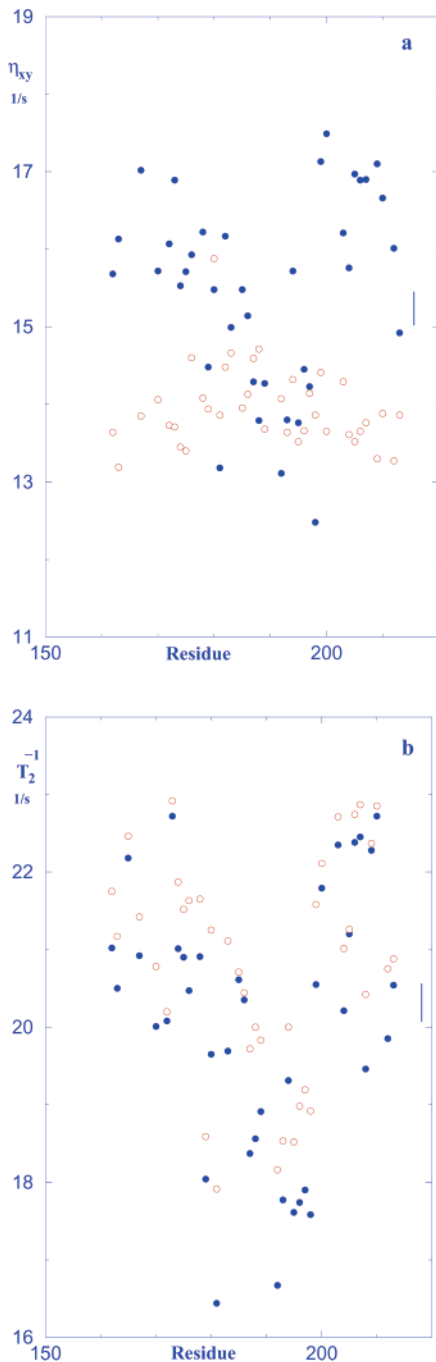


**Figure 9.** Back-calculated 14.10 T  $\eta_{xy}$  data obtained with best-fit parameters generated by  $T_1$ ,  $1/T_2 + \eta_{xy}$ , and NOE fitting (opaque red circles), superimposed on the 14.10 experimental data (solid blue circles) for the chain segment Q160–G214 of AKeco (a). Back-calculated 14.10 T  $1/T_2$  data obtained with best-fit parameters generated by  $T_1$ ,  $T_2$ , and NOE fitting (opaque red circles), superimposed on the 14.10 experimental data (solid blue circles) for the chain segment Q160–G214 of AKeco (b). Average error bars for the experimental data are depicted on the right-hand-side of the respective panels.

corresponding  $A(x)$ ,  $B(x)$ , and  $C(x)$  values are shown in Table 1. It is of interest to point out that noncollinearity between the  $^{15}\text{N}$  CSA and  $^{15}\text{N}$ – $^1\text{H}$  dipolar frames has a substantial effect, entailing a 21% [11%] reduction in  $A(\text{cc})$  [ $A(\text{cd})$ ] versus  $A(\text{dd})$ . We found previously<sup>7,13,14</sup> that  $\beta_{\text{MD}} \approx 20^\circ$  and  $\gamma_{\text{MD}} \approx -90^\circ$  are typical values associated with the ns regime. Table 1 also shows the  $A(x)$ ,  $B(x)$ , and  $C(x)$  values calculated for these data.

$U/k_{\text{B}}T$ :  $c_0^2 = 4.0$  and  $c_2^2 = 3.0$   $k_{\text{B}}T$  versus  $c_0^2 = 3.0$  and  $c_2^2 = 4.0$   $k_{\text{B}}T$ . Figure 10 illustrates the effect of parallel  $Z_{\text{M}}$  ordering

**TABLE 1: Coefficients  $A(x)$ ,  $B(x)$ , and  $C(x)$  for an Axial  $^{15}\text{N}$  CSA Tensor Obtained with  $\theta = -16^\circ$  (Ref 19), and the Euler Angles  $\Theta = (0^\circ, \beta_{\text{MD}}^\circ, \gamma_{\text{MD}}^\circ)$  for the Transformation from the DD to the M Frame<sup>a</sup>**

spectral density function	$\beta_{\text{MD}} = 0^\circ, \gamma_{\text{MD}} = 0^\circ$			$\beta_{\text{MD}} = 20^\circ, \gamma_{\text{MD}} = -90^\circ$		
	$A(x)$	$B(x)$	$C(x)$	$A(x)$	$B(x)$	$C(x)$
$J^{\text{dd}}(x)$	1.00	0.00	0.00	0.68	0.31	0.01
$J^{\text{cc}}(x)$	0.79	0.21	0.00	0.52	0.45	0.03
$J^{\text{cd}}(x)$	0.89	0.00	0.00	0.60	0.29	0.00

<sup>a</sup>  $x$  denotes dd, cc, or cd.

changing into perpendicular  $Y_{\text{M}}$  ordering. The functions  $J^x(\omega)$  (eq 11) were assembled from  $j_k(\omega)$  (eq 8) calculated with  $\mathbf{R}^{\text{C}}/\mathbf{R}_{\perp}^{\text{L}} = 0.57$ ,  $\mathbf{R}_{\parallel}^{\text{L}} \gg \mathbf{R}_{\perp}^{\text{L}}$ ,  $\tau_{\text{m}} = 15.1$  ns, and the coefficients  $A(x)$ ,  $B(x)$ , and  $C(x)$  given in Table 1 for  $\beta_{\text{MD}} = 20^\circ$  and  $\gamma_{\text{MD}} = -90^\circ$ .<sup>7,13,14</sup> The curves colored green, blue, and red are associated with  $x = \text{dd}$ ,  $\text{cc}$ , and  $\text{cd}$ , respectively. The potential associated with Figure 10a is defined by  $c_0^2 = 4.0$   $k_{\text{B}}T$  and  $c_2^2 = 3.0$   $k_{\text{B}}T$ , corresponding to  $S_0^2 = 0.55$  and  $S_2^2 = 0.232$  (eqs 4–6). The irreducible tensor components  $S_0^2$  and  $S_2^2$  were recast into the traceless Cartesian (Saupe) tensor components  $S_{xx}$ ,  $S_{yy}$ , and  $S_{zz}$ , according to  $S_{xx} = (6^{1/2}/4) S_2^2 - 1/2 S_0^2$ ,  $S_{yy} = -(6^{1/2}/4) S_2^2 - 1/2 S_0^2$ , and  $S_{zz} = S_0^2$  (ref 52). We obtained  $S_{xx} = -0.133$ ,  $S_{yy} = -0.417$ , and  $S_{zz} = 0.55$ , corresponding to parallel  $Z_{\text{M}}$  ordering and strong negative  $Y_{\text{M}}$  ordering, as  $S_{yy} = -0.417$  represents 83.4% of the extreme value of  $-0.5$ .  $X_{\text{M}}$  shows relatively weak negative alignment. The local ordering axes,  $X_{\text{M}}$ ,  $Y_{\text{M}}$ , and  $Z_{\text{M}}$ , and the main local director axis,  $Z_{\text{C}}$ , are depicted in Figure 1b, and the associated potential is illustrated in Figure 11a. This figure shows the function given by eq 3 recast as

$$U/k_{\text{B}}T = -1.5 c_0^2 \cos^2 \beta_{\text{CM}} - (3/2)^{1/2} c_2^2 \sin^2 \beta_{\text{CM}} \cos 2\gamma_{\text{CM}} \quad (15)$$

where  $\beta_{\text{MC}}$  and  $\gamma_{\text{MC}}$  denote the polar and azimuthal angles describing the orientation of the  $C$  axis in the M frame. The potential associated with the spectral densities shown in Figure 10b is defined by  $c_0^2 = 3.0$   $k_{\text{B}}T$  and  $c_2^2 = 4.0$   $k_{\text{B}}T$ , with  $S_0^2 = 0.144$  and  $S_2^2 = 0.572$ . The corresponding Cartesian tensor components are  $S_{xx} = 0.278$ ,  $S_{yy} = -0.422$ , and  $S_{zz} = 0.144$ . This potential form also has strong perpendicular  $Y_{\text{M}}$  ordering, but now  $Z_{\text{M}}$  is aligned more weakly and  $X_{\text{M}}$  shows parallel alignment. The corresponding potential form is illustrated in Figure 11b. High negative  $Y_{\text{M}}$  ordering and weak positive  $Z_{\text{M}}$  ordering, with both  $Y_{\text{M}}$  and  $Z_{\text{M}}$  lying within the peptide plane and  $\beta_{\text{MD}} \approx 20^\circ$ ,<sup>13,14</sup> restricts the equilibrium N–H orientation to the peptide plane without distorting the H–N–C $^\alpha$  angle of  $118^\circ$  (ref 53). Moreover, the local director (main  $C$  axis) can be associated with the  $\text{C}_{i-1}^\alpha$ – $\text{C}_i^\alpha$  axis or the N–C $^\alpha$  bond.

Comparison of the spectral densities shown in Figure 10, parts a and b, indicates that in general there is a change from a steeper decay in  $J^x(\omega)$  for the first case (Figure 10a) to a more gradual decay for the second case (Figure 10b). This implies a larger relative contribution of  $J^x(\omega_{\text{N}})$  in Figure 10b. For example,  $J^x(60)$  (the  $J^x(\omega_{\text{N}})$  value for 14.10 T, denoted by the vertical dotted lines) constitutes on average 57% of  $J^x(0)$  in Figure 10a and 80% of  $J^x(0)$  in Figure 10b. Thus, using potentials corresponding to high negative  $Y_{\text{M}}$  ordering will increase the back-calculated  $1/T_1$ ,  $1/T_2$ , and  $\eta_{xy}$  values and improve correspondences of the kind shown in Figure 9a. The functions  $J^{\text{dd}}(\omega)$ ,  $J^{\text{cc}}(\omega)$ , and  $J^{\text{cd}}(\omega)$  will be affected selectively, with increasing similarity between  $J^{\text{cc}}(\omega)$  and  $J^{\text{cd}}(\omega)$ . The ratio  $[J^{\text{cc}}(0) - J^{\text{cd}}(0)]/J^{\text{cd}}(0) \times 100$  is 3.8% in Figure 10a and 0.8%

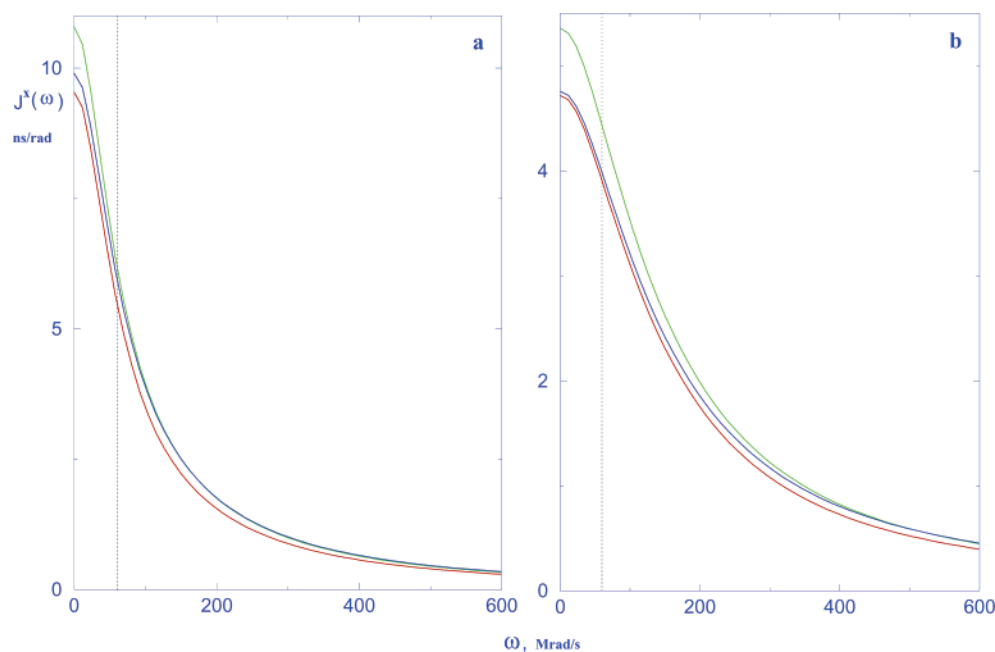


**Figure 10.** Spectral density functions  $J^{\text{dd}}(\omega)$  (green curve),  $J^{\text{cc}}(\omega)$  (blue curve), and  $J^{\text{cd}}(\omega)$  (red curve) as a function of  $\omega$  obtained from  $j_K(\omega)$  calculated with  $\mathbf{R}^{\text{C}}/\mathbf{R}_{\perp}^{\text{L}} = 0.57$ ,  $\mathbf{R}_{\perp}^{\text{L}}/\mathbf{R}_{\parallel}^{\text{L}} \rightarrow 0$ ,  $\tau_m = 15.1$  ns, and the coefficients  $A(x)$ ,  $B(x)$ , and  $C(x)$  given in Table 1 for  $\beta_{\text{MD}} = 20^\circ$ ,  $\gamma_{\text{MD}} = -90^\circ$ . (a)  $c_0^2 = 4 k_B T$  and  $c_2^2 = 3 k_B T$  [ $(S_0^2)^2 = 0.30$  and  $(S_2^2)^2 = 0.05$ ] and (b)  $c_0^2 = 3 k_B T$  and  $c_2^2 = 4 k_B T$  [ $(S_0^2)^2 = 0.02$  and  $(S_2^2)^2 = 0.33$ ]. The vertical dotted lines denote the  $\omega_N$  coordinate corresponding to a magnetic field of 14.10 T.

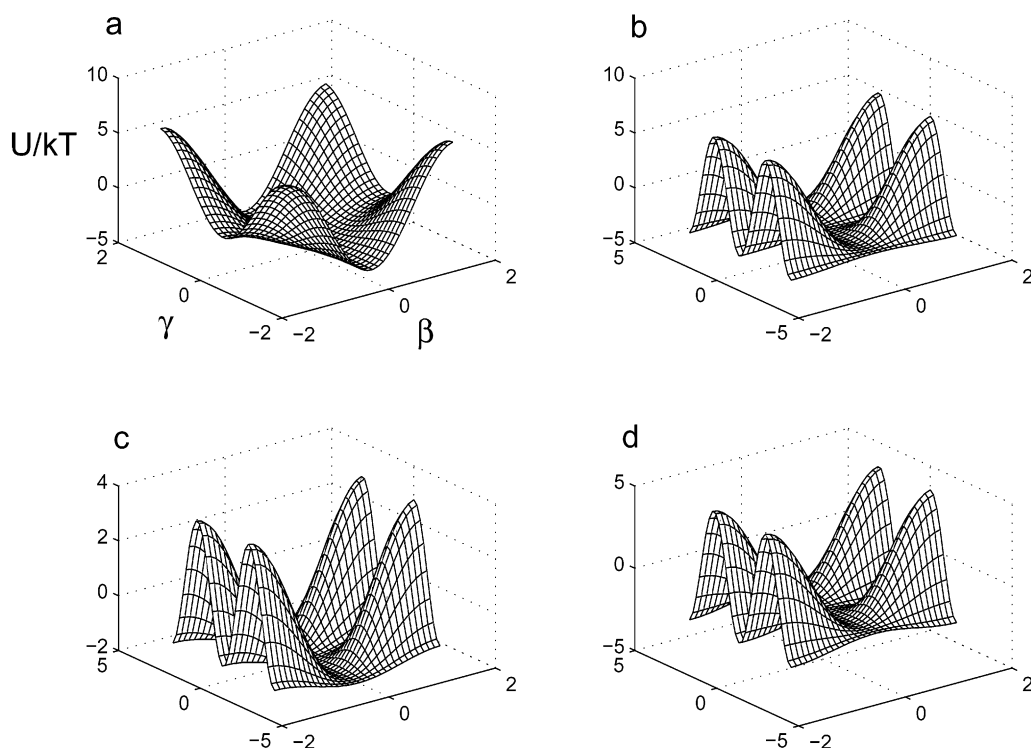


**Figure 11.** Potential function  $U/k_B T = -1.5 c_0^2 \cos^2 \beta_{\text{MC}} - (3/2)^{1/2} c_2^2 \sin^2 \beta_{\text{MC}} \cos(2\gamma_{\text{MC}})$  (eq 15) as a function of  $\beta_{\text{MC}}$  and  $\gamma_{\text{MC}}$ .  $c_0^2 = 4 k_B T$  and  $c_2^2 = 3 k_B T$  (a),  $c_0^2 = 3 k_B T$  and  $c_2^2 = 4 k_B T$  (b),  $c_0^2 = 2 k_B T$  and  $c_2^2 = 2 k_B T$  (c), and  $c_0^2 = 2 k_B T$  and  $c_2^2 = 3 k_B T$  (d). The corresponding principal values of the ordering tensor in irreducible and Cartesian form, and the related implications to the local ordering characteristics, appear in the text.

in Figure 10b. The analogous figures for  $\omega = \omega_N$  are 6.7 and 3.7%. Although the noted differences are on the order of 3% only, their effect is cumulative. Because the best-fit parameters used to reproduce  $J^{\text{cd}}(0)$  and  $J^{\text{cd}}(\omega_N)$ , which determine  $\eta_{xy}$  (eq 12), are generated by specific values of  $J^{\text{dd}}(\omega)$  and  $J^{\text{cc}}(\omega)$ , greater similarity between  $J^{\text{cc}}(\omega)$  and  $J^{\text{cd}}(\omega)$  is expected to improve correspondences of the kind shown in Figure 9a. Note that eq 11 will also feature rhombic terms for  $x = \text{dd}$  and  $\text{cd}$  in the case of asymmetric potentials. In conclusion, rhombic potentials

of the kind illustrated in Figure 11b are likely to help reconcile the noted discrepancies.

$U/k_B T$ :  $c_0^2 = c_2^2 = 2.0 k_B T$  versus  $c_0^2 = 2.0$  and  $c_2^2 = 3.0 k_B T$ . Figure 12 illustrates in further detail the effect of potential symmetry on the spectral densities. The functions  $J^x(\omega)$  shown in this figure were calculated with  $\mathbf{R}^{\text{C}}/\mathbf{R}_{\perp}^{\text{L}} = 0.57$ ,  $\mathbf{R}_{\perp}^{\text{L}} \gg \mathbf{R}_{\parallel}^{\text{L}}$ ,  $\tau_m = 15.1$  ns,  $c_0^2 = 2$  and  $c_2^2 = 2 k_B T$  [ $S_0^2 = 0.264$  and  $S_2^2 = 0.368$ ] or  $c_0^2 = 2$  and  $c_2^2 = 3 k_B T$  [ $S_0^2 = 0.088$  and  $S_2^2 =$



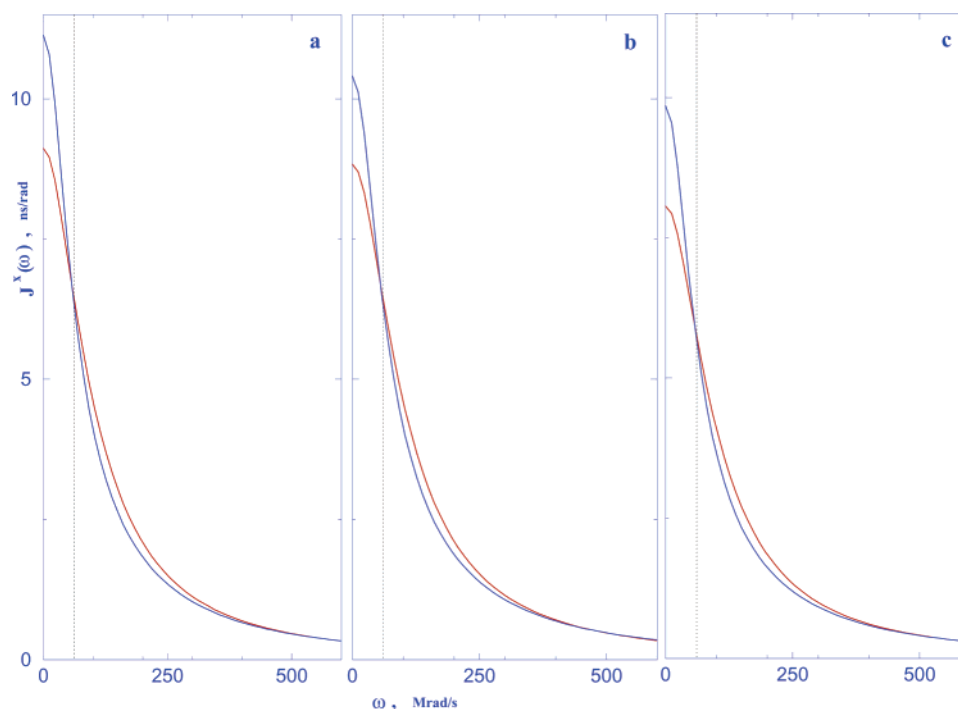


**Figure 12.** Spectral densities  $J^x(\omega)$  as a function of  $\omega$  obtained from  $j_K(\omega)$  calculated with  $\mathbf{R}^C/\mathbf{R}_\perp^L = 0.57$ ,  $\mathbf{R}_\perp^L/\mathbf{R}_\parallel^L \rightarrow 0$ ,  $\tau_m = 15.1$  ns,  $c_0^2 = c_2^2 = 2.0$   $k_B T$  [ $(S_0^2)^2 = 0.07$  and  $(S_2^2)^2 = 0.14$ ] (red curve) or  $c_0^2 = 2$   $k_B T$  and  $c_2^2 = 3$   $k_B T$  [ $(S_0^2)^2 = 0.008$  and  $(S_2^2)^2 = 0.33$ ] (blue curve), and the coefficients  $A(x)$ ,  $B(x)$ , and  $C(x)$  given in Table 1 for  $\beta_{MD} = 20^\circ$ ,  $\gamma_{MD} = -90^\circ$ . (a)  $J^{dd}(\omega)$ , (b)  $J^{cc}(\omega)$ , and (c)  $J^{cd}(\omega)$ . The vertical dotted lines denote the  $\omega_N$  coordinate corresponding to a magnetic field of 14.10 T.

0.572], and the coefficients  $A(x)$ ,  $B(x)$ , and  $C(x)$  given in Table 1 for  $\beta_{MD} = 20^\circ$  and  $\gamma_{MD} = -90^\circ$ . The potential coefficients  $c_0^2 = 2$  and  $c_2^2 = 2$   $k_B T$  correspond to the Cartesian tensor components  $S_{xx} = 0.093$ ,  $S_{yy} = -0.358$ , and  $S_{zz} = 0.265$ . This potential form, which corresponds to nearly planar  $Y_M Z_M$  alignment, is illustrated in Figure 11c. The potential coefficients  $c_0^2 = 2$  and  $c_2^2 = 3$   $k_B T$  correspond to  $S_{xx} = 0.306$ ,  $S_{yy} = -0.394$ , and  $S_{zz} = 0.088$ . This potential form, which corresponds to nearly planar  $Y_M X_M$  alignment, is illustrated in Figure 11d. The effect of nearly planar  $Y_M Z_M$  alignment changing into nearly planar  $Y_M X_M$  alignment is borne out in Figure 12. The  $J^x(\omega_N)$  values denoted by the vertical dotted lines are similar for the  $c_0^2 = c_2^2 = 2$   $k_B T$  and the  $c_0^2 = 2$  and  $c_2^2 = 3$   $k_B T$  potentials. However,  $J^x(0)$  is significantly higher in the latter case. This is precisely what Figure 9a illustrates, underestimation of  $J(0)$  when the form of the potential is inappropriate. Hence, negative  $Y_M$  ordering with nearly planar  $Y_M X_M$  alignment is selected over negative  $Y_M$  ordering with nearly planar  $Y_M Z_M$  alignment by the experimental data. It can also be seen that the relation among the  $J^x(\omega)$  values differs for  $c_2^2 = 2$  and  $c_2^2 = 3$   $k_B T$  in Figure 12. This indicates that the potential symmetry has a selective effect on the auto- and cross-correlated spectral densities.

The examples shown above indicate that  $J(0)$ , the similarity between  $J^{cc}(\omega)$  and  $J^{dd}(\omega)$ , and the ratio  $J(\omega_N)/J(0)$  will increase if data fitting is performed with rhombic potentials which correspond to negative  $Y_M$  ordering with nearly planar  $Y_M X_M$  alignment. The calculated values of  $1/T_1$ ,  $1/T_2$ , and  $\eta_{xy}$  will be augmented. Back-calculated  $1/T_2$  and  $\eta_{xy}$  data will reproduce their experimental counterparts equally well, and artificial  $R_{ex}$  terms will be eliminated. The differential effects on the auto- and cross-correlated spectral densities are expected to render  $\eta_{xy}$  particularly useful in the data fitting process.

**Summary.** The evidence in favor of  $U/k_B T$  rhombicity or  $S$  asymmetry being the dominant effect underlying the observed discrepancy between best-fit and experimental  $\eta_{xy}$  data is summarized below. It should be noted that rhombic potentials

at the N–H bond could be detected using the back-calculation technique due to  $\eta_{xy}$  being independent of  $R_{ex}$ , whereas the experimental  $1/T_2$  values depend on  $R_{ex}$ .

(1) The local potential is exerted by the local structure. There is no intrinsic reason for this potential to be axially symmetric. We found previously<sup>13,14</sup> that for slow local motions the potential at the N–H bond is rhombic. The present studies confirm this for fast local motions. The rhombic shape determined complies with the stereochemistry of the peptide plane and is in accordance with the work of Bruschweiler et al.<sup>54,55</sup> on fast local motion asymmetry.

(2)  $T_1$ ,  $T_2$ , and the NOE were back-calculated and superimposed on their experimental counterparts.  $T_1$ ,  $1/T_2 + \eta_{xy}$ , and the NOE were also back-calculated and superimposed on their experimental counterparts. Comparison indicated that incorporation of  $\eta_{xy}$  into the fitting process preserves the order parameters and reinforces fake  $R_{ex}$  terms pointing out model deficiency, which we show to consist of not accounting for potential rhombicity.

(3) For quite a few residues, the fitting is impaired when  $1/T_2$  is replaced by  $\eta_{xy}$  (see the Comments section below). Both variables are affected by potential rhombicity and both depend largely on  $J(0)$ . In the case of  $1/T_2$ , the additive term  $R_{ex}$  facilitates the fitting by absorbing potential rhombicity. This option is not available to  $\eta_{xy}$ .

(4) Spectral density functions  $J^x(\omega)$  (eq 11) were calculated for potentials corresponding to nearly planar  $Y_M X_M$  ordering, which was determined to be the particular symmetry of the potentials at the N–H bond. The change in the shapes of the  $J^x(\omega)$  functions implied by increasing rhombicity (e.g., Figure 12) explains qualitatively the current underestimation of the experimental  $\eta_{xy}$  data by the back-calculated  $\eta_{xy}$  data (Figure 9a).

**5. Physical Picture.** The following physical picture complies with the potential form elucidated based on experimental data. The orientation of the local ordering frame is defined by the

best-fit values of  $\beta_{MD} \approx 20^\circ$  and  $\gamma_{MD} \approx -90^\circ$ , which place both  $Z_M$  and  $Y_M$  in the peptide plane, also comprising the N–H bond. Data fitting led to slow peptide plane motion about  $Y_M$ , in accordance with the requirement that the M axes and the N–H bond move together. The main local ordering axis  $Y_M$  lies close to the  $C_{i-1}^\alpha - C_i^\alpha$  axis or the N– $C^\alpha$  bond,<sup>7,13,14</sup> and the extent of ordering is high. Thus, the N–H bonds are restrained to lie within the peptide plane as required by the known protein structure,<sup>53</sup> and the local director (main  $C$  axis) lies nearly perpendicular to the equilibrium N–H orientation. Low  $Z_M$  ordering preserves the known value of the H–N– $C^\alpha$  angle. High  $X_M$  ordering could be associated with the delocalized  $\pi$  orbital extending over the structural element O=C–N and may be indicative of a biaxial local director.<sup>9</sup> SRLS assumes for convenience that the local diffusion tensor is diagonal in the local ordering frame,  $M$ .<sup>7–9</sup> In accordance with the three local ordering M axes aligning differently with respect to the local director, the three local diffusion rates may also differ. The motion about  $Y_M$  was discussed above. The motion about  $Z_M$  was found to be in the extreme motional narrowing limit, hence unobservable experimentally. The best approach would be to allow the  $R^L$  tensor to be fully asymmetric.<sup>10</sup>

**6. Comments.** Several comments are in order. First of all, we found that quite a few data points could not be fit with a  $T_1$ ,  $T_2$ ,  $\eta_{xy}$ , and NOE fitting scenario, where  $\eta_{xy}$  appears as a separate variable. The artificial  $R_{ex}$  terms can accommodate experimental  $1/T_2 + \eta_{xy}$  values but are unrelated to the experimental  $\eta_{xy}$  values. This supports the rationale behind the role of  $\eta_{xy}$  in the detection of rhombic potentials. Second,  $\eta_{xy}$  was found indispensable for identifying rhombic potentials in the case of combined two-field data fitting. When multifield data are combined, a large number of high-frequency  $J(\omega)$  values are featured. In this case, the local dynamics information content of the latter may suffice to bear out the underestimation of  $J(0)$  implied by using axial potential in data fitting, whereas the actual potentials are rhombic with nearly planar  $Y_M X_M$  ordering. This might have been the case in ref 56, where a missing  $J(0)$  contribution, which could be reconciled by eliminating  $T_2$  from the analysis, was reported for four-field Ubiquitin data analyzed in concert. Third, as shown above, asymmetric potentials increase the relaxation rates  $\eta_{xy}$  and  $1/T_2$ , perforce increasing the respective experimental errors (see chain region 55–59 and 102–107 in Figure 3, parts a and b). Therefore, statistical analyses of the product  $(\eta_{xy}) \times (T_2)$  may miss information extractable by considering  $\eta_{xy}$  and  $^{15}N$   $T_2$  separately. Finally, significant recent advances in protein NMR were made possible by the development of transverse relaxation optimized spectroscopy (TROSY).<sup>22,23</sup> The respective line widths are given by the difference  $1/T_2 - \eta_{xy}$ . On the basis of the present study, both  $1/T_2$  and  $\eta_{xy}$  can be calculated for slow local motions and rhombic potentials. Hence, TROSY line widths are generally predictable using SRLS.

This constitutes an interpretation of our findings in terms of the shape of the potential  $U/k_B T$ . An interpretation wherein the absolute values of  $c_0^2$  and  $c_2^2$  are determined requires incorporation of rhombic potentials into the fitting scheme for SRLS, an effort that is currently underway.

## Conclusions

The mode-coupling SRLS approach has been applied to transverse  $^{15}N$  CSA– $^{15}N$ – $^1H$  dipolar cross-correlated relaxation,  $\eta_{xy}$ . For the first time  $\eta_{xy}$  data associated with chain segments experiencing slow local motion, which are typically the biologically relevant ones, are amenable to investigation. Experimental

$\eta_{xy}$  values of RNase and AKeco could not be reproduced from best-fit parameters generated by data fitting that used axial potentials. Calculations showed they are reproducible using rhombic potentials. The form of the latter was established as perpendicular negative  $Y_M$  ordering with positive  $X_M$  alignment preferred over positive  $Z_M$  alignment. The extent of negative  $Y_M$  ordering is high, and the extent of  $Z_M$  ordering is low, largely preserving the known in-peptide-plane N–H bond vector orientation. The local director is associated with the  $C_{i-1}^\alpha - C_i^\alpha$  axis (or the N– $C^\alpha$  bond). Accurate determination of the potential coefficients  $c_0^2$  and  $c_2^2$  is expected to be accomplished with concerted fitting of auto- and cross-correlated  $^{15}N$  relaxation rates using a fitting scheme based on rhombic potentials. This development is in progress. When axial potentials are used to fit the data, then the actual potential rhombicity must be absorbed by an artificial  $R_{ex}$  term. Therefore, best-fit  $R_{ex}$  data obtained with axial potentials should be considered carefully. Back-calculation is useful for identifying inappropriate elements of the dynamic model, and can thereby help improve it.

**Acknowledgment.** This work was supported by the Israel Science Foundation grant number 520/99-16.1 to E.M., the Damadian Center for Magnetic Resonance research at Bar-Ilan University, and a Grant from NIH/NCRR to J.H.F. E.M. gratefully acknowledges the hospitality of CCBB, University of Pittsburgh Medical School, Pittsburgh, PA, where she spent her sabbatical year 2002/2003, in the course of which this work was finalized.

## References and Notes

- (1) Kay, L. E. *Nat. Struct. Biol.* **1998**, *5*, 513–517.
- (2) Ishima, R.; Torchia, D. A. *Nat. Struct. Biol.* **2000**, *7*, 740–743.
- (3) Peng, J. W.; Wagner, G. In *Methods in Enzymology*; James, T. L., Oppenheimer, N. J., Eds.; Academic Press: New York, 1994; Vol. 239, pp 563–595.
- (4) Lipari, G.; Szabo, A. *J. Am. Chem. Soc.* **1982**, *104*, 4546–4559.
- (5) Lipari, G.; Szabo, A. *J. Am. Chem. Soc.* **1982**, *104*, 4559–4570.
- (6) Clore, G. M.; Szabo, A.; Bax, A.; Kay, L. E.; Driscoll, P. C.; Gronenborn, A. M. *J. Am. Chem. Soc.* **1990**, *112*, 4989–4991.
- (7) Tugarinov, V.; Liang, Z.; Shapiro, Y. E.; Freed, J. H.; Meirovitch, E. *J. Am. Chem. Soc.* **2001**, *123*, 3055–3063.
- (8) Polimeno, A.; Freed, J. H. *Adv. Chem. Phys.* **1993**, *83*, 89–210.
- (9) Polimeno, A.; Freed, J. H. *J. Phys. Chem.* **1995**, *99*, 10995–11006.
- (10) Liang, Z.; Freed, J. H. *J. Phys. Chem. B* **1999**, *103*, 6384–6396.
- (11) Barnes, J. P.; Liang, Z.; Mchaourab, H. S.; Freed, J. H.; Hubbell, W. L. *Biophys. J.* **1999**, *76*, 3298–3306.
- (12) Liang, Z.; Freed, J. H.; Keyes, R.; Bobst, A. M. *J. Phys. Chem. B* **2000**, *104*, 5372–5381.
- (13) Tugarinov, V.; Shapiro, Y. E.; Liang, Z.; Freed, J. H.; Meirovitch, E. *J. Mol. Biol.* **2002**, *315*, 171–186.
- (14) Shapiro, Y. E.; Kahana, E.; Tugarinov, V.; Liang, Z.; Freed, J. H.; Meirovitch, E. *Biochemistry* **2002**, *41*, 6271–6281.
- (15) Goldman, M. *J. Magn. Res.* **1984**, *60*, 437–452.
- (16) Tjandra, N.; Szabo, A.; Bax, A. *J. Am. Chem. Soc.* **1996**, *118*, 6986–6991.
- (17) Kroenke, C. D.; Loria, J. P.; Lee, L. K.; Rance, M.; Palmer, A. G., III. *J. Am. Chem. Soc.* **1998**, *120*, 7905–7915.
- (18) Fushman, D.; Cowburn, D. *J. Am. Chem. Soc.* **1998**, *120*, 7109–7110.
- (19) Fushman, D.; Tjandra, N.; Cowburn, D. *J. Am. Chem. Soc.* **1998**, *120*, 10947–10952.
- (20) Kroenke, C. D.; Rance, M.; Palmer, A. G., III. *J. Am. Chem. Soc.* **1999**, *121*, 10119–10125.
- (21) Fushman, D.; Tjandra, N.; Cowburn, D. *J. Am. Chem. Soc.* **1999**, *121*, 8577–8582.
- (22) Pervushin, K.; Riek, R.; Wider, G.; Wuthrich, K. *Proc. Natl. Acad. Sci. U.S.A.* **1997**, *94*, 12366–12371.
- (23) Pervushin, K.; Riek, R.; Wider, G.; Wuthrich, K. *J. Am. Chem. Soc.* **1998**, *120*, 6394–6400.
- (24) Fushman, D.; Cowburn, D. *J. Biomol. NMR* **1999**, *13*, 139–147.
- (25) Fischer, M. W. F.; Zeng, L.; Pang, Y.; Hu, W.; Majumdar, A.; Zuiderweg, E. R. P. *J. Am. Chem. Soc.* **1997**, *119*, 12629–12642.
- (26) Pellecchia, M.; Pang, Y.; Wang, L.; Kurochkin, A. V.; Kumar, A.; Zuiderweg, E. R. P. *J. Am. Chem. Soc.* **1999**, *121*, 9165–9170.

- (27) Pang, Y.; Zuiderweg, E. R. P. *J. Am. Chem. Soc.* **2000**, *122*, 4841–4842.
- (28) Freed, H. J.; Nayeem, A.; Rananavare, S. B. *The Molecular Dynamics of Liquid Crystals*; Luckhurst, G. R., Veracini, C. A., Eds.; Kluwer Academic Publishers: The Netherlands, 1994; Chapter 12, pp 271–312.
- (29) Freed, J. H. *Spin Labeling: Theory and Applications*; Berliner, L. J., Ed.; Academic Press: New York, 1976; p 53.
- (30) Abragam, A. *Principles of Nuclear Magnetism*, Oxford University Press: Clarendon: London, 1961.
- (31) Reinstein, J.; Brunne, M.; Wittinghofer, A. *Biochemistry* **1988**, *27*, 4712–4720.
- (32) Sinev, M. A.; Sineva, E. V.; Ittah, V.; Haas, E. *FEBS Lett.* **1996**, *397*, 273–276.
- (33) Giron, I. S.; Gilles, A.-M.; Margarita, D.; Michelson, S.; Monnot, M.; Femandjian, S.; Danchin, A.; Barzu, O. *J. Biol. Chem.* **1987**, *262*, 622–629.
- (34) Shapiro, Y. E.; Sinev, M. A.; Sineva, E. V.; Tugarinov, V.; Meirovitch, E. *Biochemistry* **2000**, *39*, 6634–6664.
- (35) Delaglio, F.; Grzesiek, S.; Vuister, G. W.; Zhu, G.; Pfeifer, J.; Bax, A. *J. Biomol. NMR*, **1995**, *6*, 277–293.
- (36) Burlacu-Miron, S.; Perrier, V.; Gilles, A.-M.; Mispelter, J.; Barzu, O.; Craescu, C. T. *J. Biomol. NMR* **1999**, *13*, 93–94.
- (37) Vold, R. L.; Waugh, J. S.; Klein, M. P.; Phelps, D. E. *J. Chem. Phys.* **1968**, *48*, 3831–3832.
- (38) Meiboom, S.; Gill, D. *Rev. Sci. Instrum.* **1958**, *29*, 688–691.
- (39) Noggle, J. H.; Shirmer, R. E. *The Nuclear Overhauser Effect: Chemical Application*; Academic Press: New York, 1971.
- (40) Kay, L. E.; Nicholson, L. K.; Delaglio, F.; Bax, A.; Torchia, D. A. *J. Magn. Res.* **1992**, *97*, 359–375.
- (41) Palmer, A. G., III.; Skelton, N. J.; Chazin, W. J.; Wright, P. E.; Rance, M. *Mol. Phys.* **1992**, *75*, 699–711.
- (42) Grzesiek, S.; Bax, A. *J. Am. Chem. Soc.* **1993**, *115*, 12593–12594.
- (43) Live, D. H.; Davis, D. G.; Agosta, W. C.; Cowburn, D. *J. Am. Chem. Soc.* **1984**, *106*, 1939–1941.
- (44) Palmer, A. G., III.; Rance, M.; Wright, P. E. *J. Am. Chem. Soc.* **1991**, *113*, 4371–4380.
- (45) Press, W. H.; Teukolsky, S. A.; Vetterling, W. T.; Flannery, B. P. *Numerical Recipes in C. The Art of Scientific Computing*; Cambridge University Press: New York, 1992.
- (46) Kamath, U.; Shriver, J. W. *J. Biol. Chem.* **1989**, *264*, 5586–5592.
- (47) Mandel, A. M.; Akke, M.; Palmer, A. G., III. *Biochemistry* **1996**, *35*, 16009–16023.
- (48) Bruschweiler, R.; Liao, X.; Wright, P. E. *Science* **1995**, *268*, 886–889.
- (49) Lee, L. K.; Rance, M.; Chazin, W. J.; Palmer, A. G., III. *J. Biomol. NMR* **1997**, *9*, 287–298.
- (50) Sinev, M. A.; Sineva, E. V.; Ittah, V.; Haas, E. *Biochemistry* **1996**, *35*, 6425–6437.
- (51) Vasadava, K. V.; Schneider, D. S.; Freed, J. H. *J. Chem. Phys.* **1987**, *86*, 647–661.
- (52) Meirovitch, E.; Igner, D.; Igner, E.; Moro, G.; Freed, J. H. *J. Chem. Phys.* **1982**, *77*, 3915–3938.
- (53) Schulz, G. E.; Schirmer, R. H. In *Principles of Protein Structure*; Cantor, C. R., Ed.; Springer-Verlag: New York, 1990; p 18.
- (54) Bruschweiler, R.; Liao, X.; Wright, P. E. *Science* **1995**, *268*, 886–889.
- (55) Lienin, S. F.; Bremi, T.; Brutscher, B.; Bruschweiler, R.; Ernst, R. *J. Am. Chem. Soc.* **1998**, *120*, 9870–9879.
- (56) Lee, A. L.; Wand, J. *J. Biomol. NMR* **1999**, *13*, 101–112.